Hindawi
Journal of Electrical and Computer Engineering
Volume 2018, Article ID 1328736, 25 pages
https://doi.org/10.1155/2018/1328736

Research Article

Harmonic Susceptibility Study of DC Collection Network Based on Frequency Scan and Discrete Time-Domain Modelling Approach

Carlos Enrique Imbaquingo, Eduard Sarrà, Nicola Isernia, Alberto Tonellotto, Yu-Hsing Chen, Catalin Gabriel Dincan, Philip Kjær, Claus Leth Bak, and Xiongfei Wang

Department of Energy Technology, Aalborg University, Aalborg, Denmark

Correspondence should be addressed to Catalin Gabriel Dincan; cgd@et.aau.dk

Received 19 July 2018; Revised 31 October 2018; Accepted 6 November 2018; Published 16 December 2018

Guest Editor: Luigi P. Di Noia

The equivalent model of offshore DC power collection network for the harmonic susceptibility study is proposed based on the discrete time-domain modelling technique and frequency scan approach in the frequency domain. The proposed methodology for modelling a power converter and a DC collection system in the frequency domain can satisfy harmonic studies of any configuration of wind farm network and thereby find suitable design of power components and array network. The methodology is intended to allow studies on any configuration of the wind power collection, regardless of choice of converter topology, array cable configuration, and control design. To facilitate harmonic susceptibility study, modelling DC collection network includes creating the harmonic model of the DC turbine converter and modelling the array network. The current harmonics within the DC collection network are obtained in the frequency domain to identify the resonance frequency of the array network and potential voltage amplification issues, where the harmonic model of the turbine converter is verified by the comparison of the converter switching model in the PLECS™ circuit simulation tool and laboratory test bench, and show a good agreement.

1. Introduction

Offshore wind power is becoming an important energy resource in Europe. However, electrical power losses are always a concern in the operation of wind farm with long-range power transmission. To reduce losses, researchers look to replace AC with DC in the entire path from the wind turbine, through power collection and transmission to shore. Medium-voltage DC (MVDC) collection of wind power is an attractive solution to reduce overall losses and installation cost [1, 2]. The article [2] addresses cost-efficient solution to form the multiterminals of DC grid with the diode rectifier unit (DRU). However, the solution of DRU can produce a considerable harmonic current within the array network if the 6-pulse DRU topology is used.

Figure 1 illustrates a DC collection network of radial type of offshore wind farm with the HVDC transmission. This general configuration in Figure 1 supports any choice of MVDC collector voltage level as well as converter topology and the number of wind power plant (WPP) clusters. For example, the turbine and offshore substation can employ any DC/DC converter topology with multiple degrees of freedom: uni- vs bidirectional power flow; modular (parallel/series connection) vs monolithic; topology (single active bridge, dual active bridge, and more [3–5]). Figures 1 and 2 illustrate the details of wind farm configuration including wind turbine DC/DC converters, offshore substation converters, and onshore substation converters. The offshore wind farm is designed to generated and deliver 700 MW power from offshore to onshore [1].

The series resonant converter (SRC#) is selected as the turbine DC/DC converter based on the converter efficiency, high-voltage transfer ratio, scale of converter, and galvanic isolation property. Considering the existing converter topology and its power rating in high-power applications, the modular multilevel converter (MMC) with the galvanic isolation and unidirectional power flow control is selected to serve as the offshore substation converter to deliver the

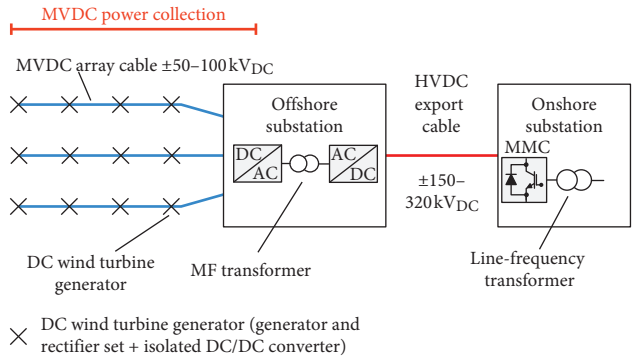

Figure 1: General configuration of the wind power plant with MVDC power collection.

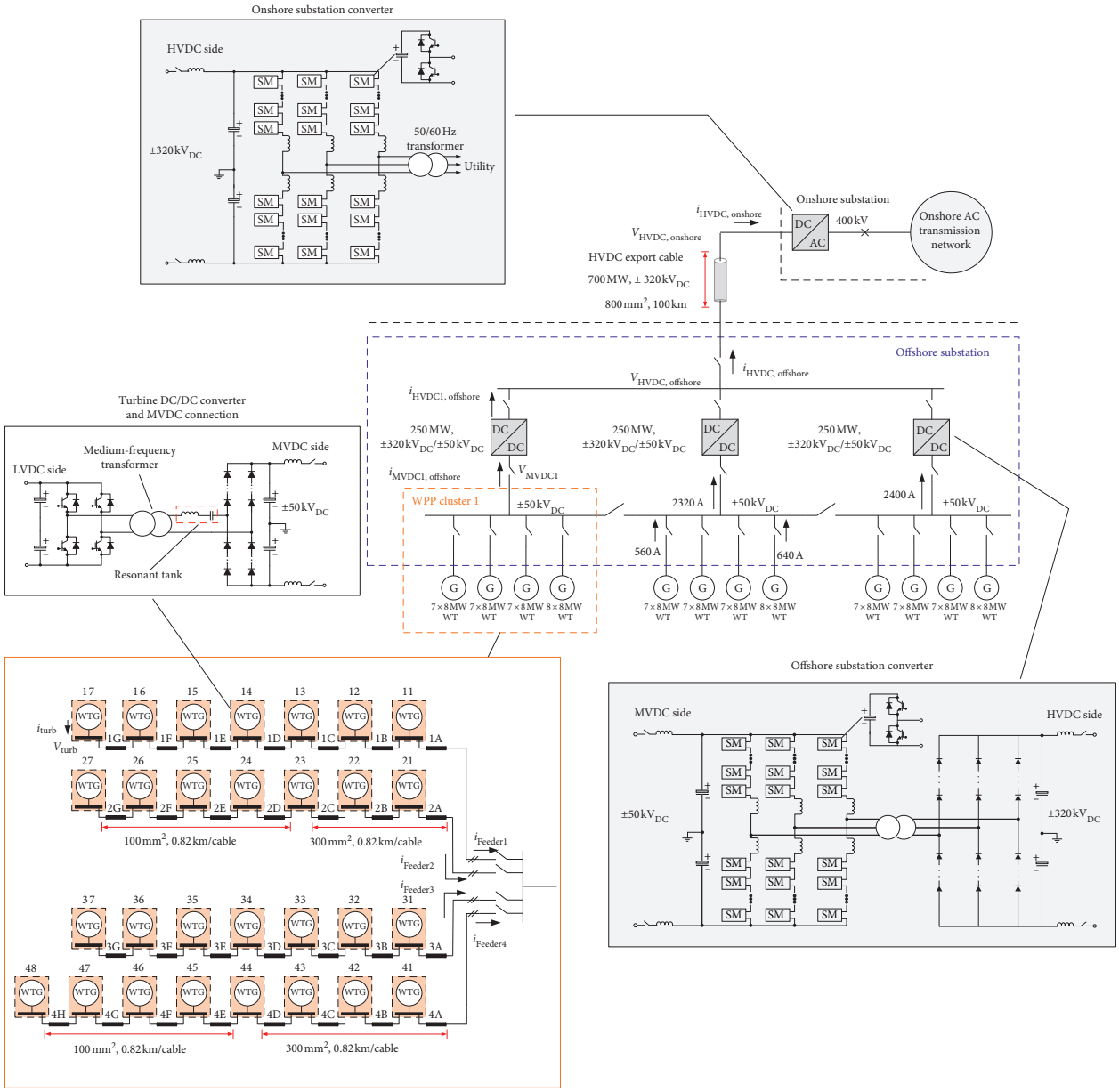

Figure 2: Single line diagram of example 700 MW offshore DC wind farm [1].

offshore wind power to the onshore grid via the HVDC transmission line. The onshore substation captures the power from the offshore wind farm by the onshore MMC with a grid-connected 50/60 Hz transformer. The onshore substation is designed to match with onshore AC grid voltage (utility) and deliver the offshore power to the onshore AC transmission network and alleviate the influence from the grid fault.

In this study, a series resonant converter topology (named SRC#) shown in Figure 3 is selected as the candidate for DC power conversion via $\pm 50\,kV_{DC}$ MVDC array network. With the series resonant converter, the DC turbine converter can take advantages of high efficiency, high-voltage transformation ratio, and galvanic fault isolation for different ratings of turbine generator [6–9]. A series resonant converter SRC# with the resonant tank on the secondary side and governed by the phase shift and a frequency-depended power flow control technique is here considered [10, 11].

To synthesize the DC-connected wind turbine converter and the MVDC gird, the wind turbine converter has to meet the following requirements:

(1) Control of the LVDC bus

(2) High-voltage transformation from the LVDC to MVDC

(3) Galvanic isolation

(4) Roust and compact design

Large amount of possible topology of converter topologies for a DC turbine is investigated. However, all of existing converter designs are immature technology, thus selecting an optimal topology is not a straightforward solution for converter design [12]. The turbine converter is designed to deliver the captured wind energy produced by the generator to the MVDC gird and then control the LVDC bus. Regarding power rating, number of components, and the possible solution of the turbine converter topologies in the early DC wind farm design, the hard-switched full-bridge power converter is selected as preferred topology [4, 13–17]. Therefore, the proposed series resonant converter # (SRC#) combined with the medium-frequency transformer (MF transformer) which serves as the DC turbine converter is selected to boot the low-voltage DC (LVDC) to high-voltage DC (MVDC-side of SRC#) with a high-voltage transferring ratio and provides a galvanic isolation to make sure that the line is immune from line faults [4, 18, 19].

The concept of SRC is widely used in the traction applications, which is usually operated at constant frequency and subresonant mode to archive a roust and compact design target in high-voltage specifications [20–24]. One of famous modulation techniques (or topologies) is the half-cycle discontinuous-conduction-mode series resonant converter (HC-DCM-SRC). Under the traction applications, the DC/DC converter is tied between two DC voltages with a fixed voltage transfer ratio and the open-loop control. Relying on the pulse removal technique, the bulky transformer in the classic SRC can be voided in the proposed SRC#, and thus the compact convert design can be archived [25]. More details of operation principle of SRC# is addressed Section 2.

To archive the study of harmonic susceptibility in offshore wind farm with the selected turbine converter, the analysis of array network in wind farm includes modelling the selected turbine converter (SRC#), array cable, and substation converter, where the substation converter in this study is considered as an ideal voltage source to produce DC component of MVDC and harmonic components. The objective of the study is to investigate how the harmonic affects the turbine converter and array networks. In the power collection system, the wind turbines and substation are connected together by medium-voltage DC cables. However, there are no standards or guidelines for such DC array network design, and thus some studies are still made by simply selecting commercially available medium-voltage AC submarine cables without giving any additional consideration in the cable's properties such as insulation [26].

Modelling of the array cables is an essential task for evaluating results of cable sizing by computer simulation. The complexity of modelling is dependent on the phenomenon, which will be conducted in the study case. For example, the travelling waves (voltage and current) with a finite propagation speed cause reflections. This phenomenon has to be represented on the cable model when study cases are intended to conduct the overvoltage or switching transient issues. Typically, three types of cable models, Pi Model, Bergeron model, and frequency-dependent models, which are available in the electromagnetic transient simulation program PSCAD™ (EMTDC) for studying AC and DC power collection systems are used [27–30]. To adequately represent the cable parameters for the harmonic susceptibility studies over different frequency ranges, the frequency-dependent array cable models are generated from geometric cable data based on the method [31] and recommendations proposed by the articles [32] and verified by the generated cable model in PSCAD™.

Although these DC alternatives promise lower electrical losses and lower bill-of-material, it is still an immature technology. As the many existing AC wind power plants, the harmonic pollution is an important issue since wind power collection systems serve by large amount of turbine converters [33–36]. Depending on the configuration of the wind power plant, every power collection system has its own inherent resonance behavior. The network, which is rich in the harmonic current, can increase the power losses and the stress of power components and cause unpredicted equipment trip. The resonance behavior inside the collection network is affected by properties of the array cable, filter designs, converter topologies, and PWM schemes. Therefore, the objective of this paper is to develop a methodology to identify potential harmonic resonant problems in the DC collection network. For example, the phenomenon of harmonic amplification relates to grid contingencies, variation of load flow, cable length, and uncertainties of network [33, 37]. The article [38] focuses on the stability issues of DC grid related to the travel waves on the transmission line and harmonic content of converters. The paper identifies the travelling wave in the long submarine array cable

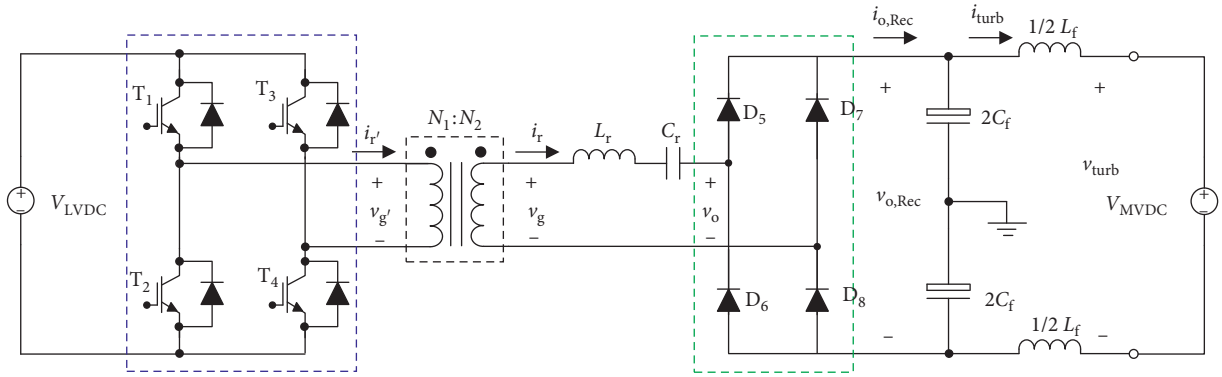

Figure 3: Circuit topology of the DC wind turbine converter (SRC#).

and resonant problem between the cable length and the switching action of the substation converter. According to the practical cases, the DC wind farm topologies for the case study mainly focus on the offshore wind farm with a short DC power transmission path.

Reviewing the common techniques for wind farm analysis, the frequency scan techniques are usually used for identifying harmonic voltage distortion of specific harmonic component in wind farms [34, 39, 40]. In this case, the wind turbines are represented for a specific frequency with an admittance equivalent circuit. The array cable model is selected according to the cable length and interesting frequency ranges of harmonic analysis. To adequately represent the cable parameters in the study, both equivalent PI section and frequency-dependent phase model are *generally* used to consider the frequency dependence of the cable parameters [28, 31, 41]. Additionally, the wind farm configuration could be changed via the operation of disconnectors or circuit breakers due to maintenance or forced outages of fault. Therefore, the harmonic study of wind farm must include all agreed switching configuration [39].

2. Review of Operation Principle of Series Resonant Converter

The circuit topology of series resonant converter # (SRC#) with the medium-frequency transformer is depicted in Figure 3, and the topology comprises a full-bridge inverter, a medium-frequency transformer, resonant LC tank, and medium-voltage output diode rectifier. The switch pairs T_1 (leading leg) and T_2 and T_3 (lagging leg) and T_4 operate at a 50% duty cycle as in Figure 4(e). Commutation of switches on the leading leg (T_1, and T_2) is shifted by an angle of δ, which is respect to the conduction of the switches on the lagging leg (T_3, and T_4). The duration of phase shift equals to half cycle of the L_rC_r tank resonant period, resulting in a quasisquare excitation voltage as seen in Figure 4(a), and then, the voltage passes through the medium-frequency transformer and excites L_rC_r resonant tank where the resonant tank current i_r is given in Figure 4(b). Via the diode rectifier and the output filter, the current (or power) is delivered to the medium-voltage network, V_{MVDC}. Up to this point, there is no difference in the operation compared to a constant frequency and phase-shift control of classical SRC, which is usually operated in the *super resonant mode*, to achieve ZVS at turn on.

Considering the switching losses with IGTB applications, the subresonant mode is preferred in SRC# which allows *ZCS* or a *low current at turnoff* (Figure 5(a)); regardless of switching frequency, a full-resonant current pulse is delivered to the load [12]. The control law of SRC# is also allowed *ZVS at turnon* and *ZCS at turnoff* for the diode rectifier, as shown in Figure 5(b). It should be noted that the output power has a positive relation with the switching frequency, which means that the output power depends how much energy (current pulse) transfers to the output stage. SRC# operated in a low frequency means lower output power, while high-frequency operation will deliver a higher output power.

3. Linearized Model and Closed-Loop Control of Series Resonant Converter

The objective of the study is to understand the harmonics distribution of offshore DC wind farm and how the DC wind turbines are affected by harmonics from the MVDC gird. Figure 6 summarizes the derivation of the plant model of the DC wind turbine based on the discrete time-domain modelling approach (Steps 1–8) [42], the transfer function of the output LC filter (Step 9), and SRC#'s control design (Steps 10–12). The details of the derivation (or equations) are address in Appendices A, B, and C which can help reader to reach the harmonic model of the DC wind turbine and then conduct harmonic susceptibility study of the DC wind farm. The following discussion including the flow chart only shows most important conclusions (or equations) of the derivation due to the limitation of page length.

The ideal of the harmonic model of the DC wind turbine converter is developed based on the harmonic model of the AC wind turbine and linearized model of the series resonant converter (SRC#) with discrete time-domain modelling approach [42, 43]. A linearized state-space model of SRC# in subresonant mode is reported in (1) and in (A.37) in Appendix:

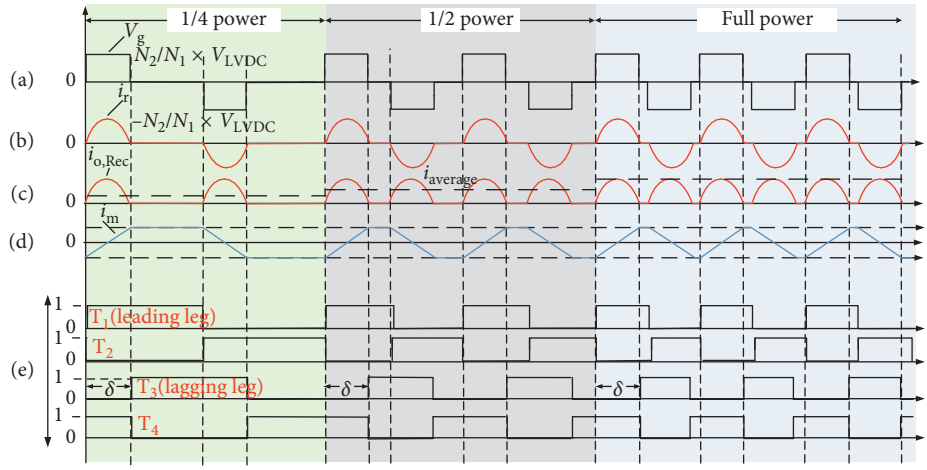

FIGURE 4: Operation waveform of SRC#: (a) inverter output voltage V_g; (b) resonant tank current i_r; (c) rectifier output current $i_{o,Rec}$ and output averaged current $i_{average}$; (d) transformer magnetizing current i_m; (e) switching patterns (T_1, T_2, T_3, and T_4) [12].

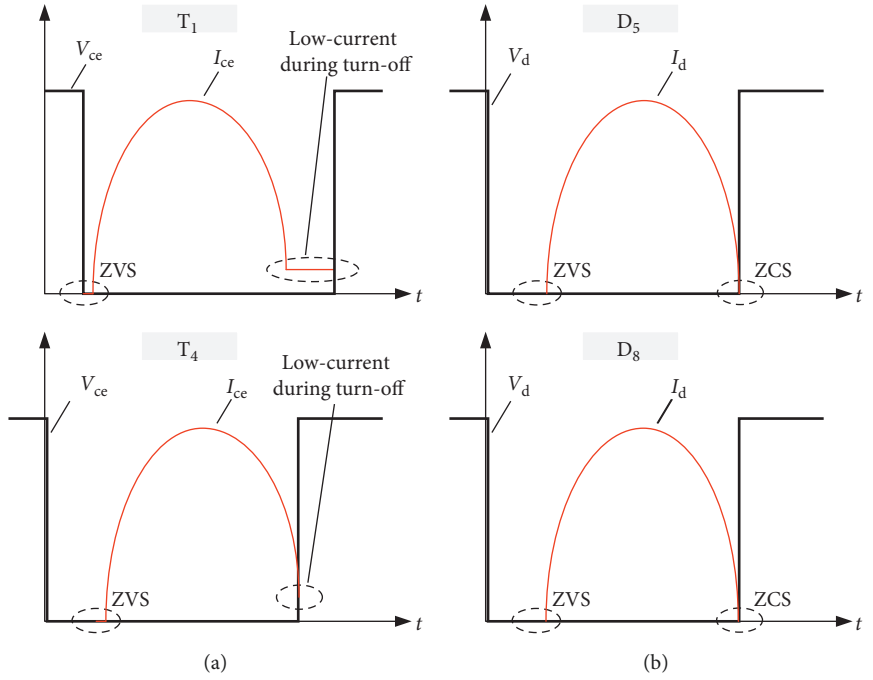

FIGURE 5: Current waveform during switching of SRC# [12]. (a) Example of *ZCS* or a small current at turnoff: switching waveforms T_1 and T_4 IGBTs. (b) Example of *ZCS* at turn-off for the rectifier diodes: switching waveforms D_5 and D_8 diodes.

$$\begin{bmatrix} \dot{\tilde{x}}_1 \\ \dot{\tilde{x}}_2 \end{bmatrix} = [A] \begin{bmatrix} \tilde{x}_1 \\ \tilde{x}_2 \end{bmatrix} + [B] \begin{bmatrix} \tilde{f}_s \\ \tilde{V}_g \\ \tilde{V}_o \end{bmatrix},$$
$$\tilde{I}_o = [C] \begin{bmatrix} \tilde{x}_1 \\ \tilde{x}_2 \end{bmatrix} + [D] \begin{bmatrix} \tilde{f}_s \\ \tilde{V}_g \\ \tilde{V}_o \end{bmatrix}, \quad (1)$$

where $\tilde{x}_1 = \tilde{I}_r$ and $\tilde{x}_2 = \tilde{v}_{cr}$.

It is enough to recall here that the duty cycle is fixed to 50%, and one event is defined as a whole time interval in which the IGBT T_1 is pulsed or not, lasting half of the switching period [10]. The state variables are meaningful of the tank current and resonant capacitor voltage at the beginning of one event, while the rectified output current is averaged over one event. The average output current is regulated by the proper action of the switching frequency. Transfer functions between converter output current and input variables are

$$\tilde{I}_{o,Rec}(s) = [\, g_1(s) \;\; g_2(s) \;\; g_3(s) \,] \begin{bmatrix} \tilde{f}_s \\ \tilde{V}_g \\ \tilde{V}_o \end{bmatrix}. \quad (2)$$

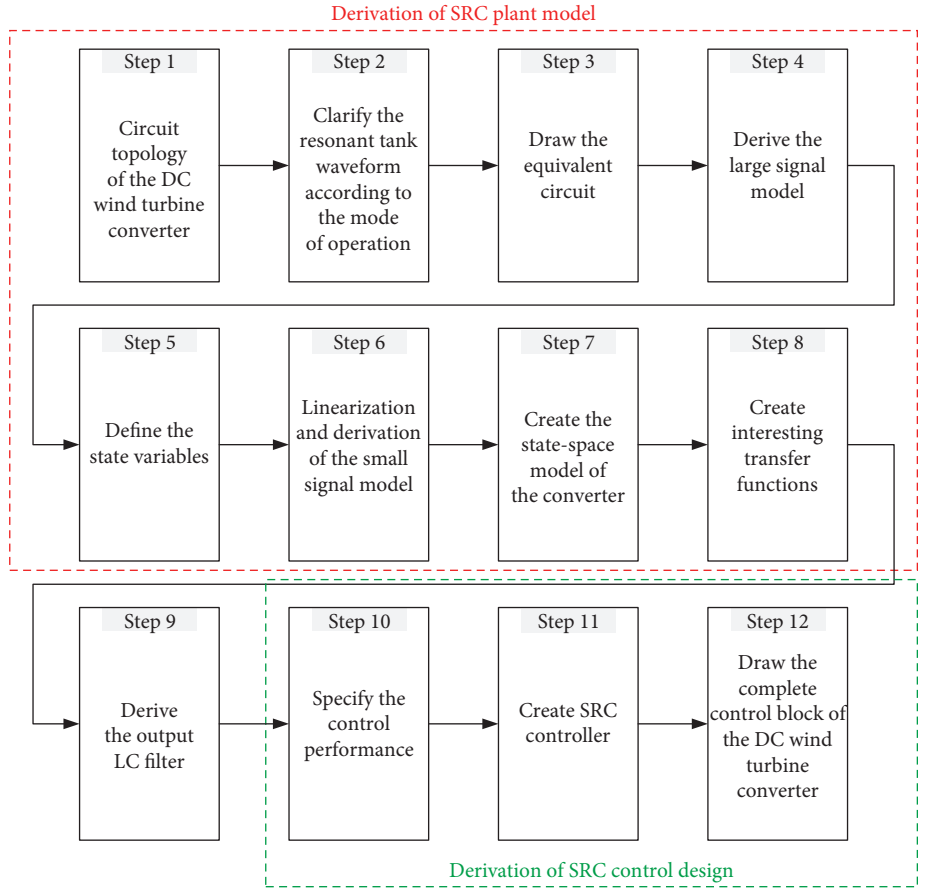

Figure 6: Flow chart of mathematical derivation of the converter plant model and the digital controller.

The transfer function between output current and input variables (i.e., $g_1(s)$, $g_2(s)$, and $g_3(s)$) can be obtained via

$$[\, g_1(s) \;\; g_2(s) \;\; g_3(s) \,] = C(sI - A)^{-1}B + D, \tag{3}$$

where

$$g_1(s) = \left.\frac{\tilde{I}_{o,Rec}(s)}{\tilde{f}_s(s)}\right|_{\tilde{V}_o(s),\tilde{V}_g(s)=0},$$

$$g_2(s) = \left.\frac{\tilde{I}_{o,Rec}(s)}{\tilde{V}_g(s)}\right|_{\tilde{f}_s(s),\tilde{V}_o(s)=0}, \tag{4}$$

$$g_3(s) = \left.\frac{\tilde{I}_{o,Rec}(s)}{\tilde{V}_o(s)}\right|_{\tilde{f}_s(s),\tilde{V}_g(s)=0}.$$

Those transfer functions describe how the averaged output current of the converter, before the output LC filter, is influenced by input disturbances. Regarding the voltage harmonics in the array network (MVDC network), the transfer function $g_3(s)$ can be used to evaluate the effect of the voltage harmonics on the converter output current. Detailed derivation of the linearized state-space model for SRC# from (1) to (3) and control design including the expression of elements in $[A]$, $[B]$, $[C]$, and $[D]$ matrixes are revealed in Appendix.

The output LC filter is designed with the natural frequency of 100 Hz (i.e., $f_f = 1/(2\pi\sqrt{(L_f C_f)}) \approx 100$ Hz) in order to have constant power delivered to the MVDC grid and attenuate high frequency harmonics, around twice the switching frequency. Based on the plant model of SRC#, the transfer function of the compensator (or controller) $g_c(s)$ in the control block shown in Figure 7 for a specific operating point (OP) is set as

$$g_c = \frac{K}{s \cdot \left(1 - \left(s/\omega_p\right)\right)}. \tag{5}$$

The transfer function g_c in (5) is designed based on predetermined specifications, such as the ability to reach its reference output current with least ringing, overshoot, and fastest dynamic during perturbations in input variables. The compensator is composed by an integrator to minimize the steady-state error, a pole around the resonant frequency of the filter to lower the resonant magnitude peak influence (ω_p), and finally a gain K, necessary to set a proper crossover frequency, which in this case needs to be lower than the resonant frequency of the filter to avoid instability. Control deign of SRC# is revealed in Appendix, and the parameters of the controller are described in Section 6 that operates in the working conditions specified in Table 1 are shown in Table 2.

Figure 8 demonstrates the transfer function $g_c(s)$ at the operation point ($\omega_p = -250$ rad/s, $K = 50.8$ dB, and $P_{out} = 12.7$ MW). The result shows that the gain margin G_M is

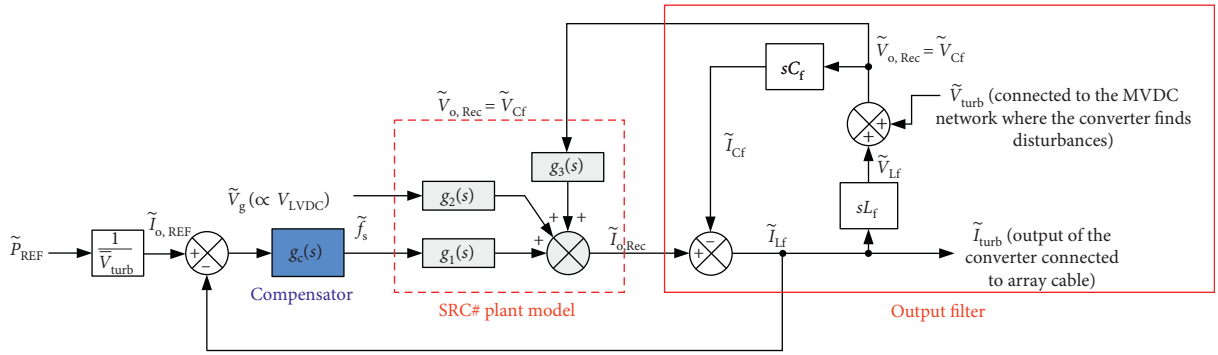

Figure 7: Block diagram of the the DC wind turbine converter (SRC#) in the closed-loop control with the output filter.

Table 1: Parameters of the plant model of SRC#.

Turns ratio of transformer ($N_1 : N_2$)	1 : 25
Resonant inductor, L_r	78.1 (mH)
Resonant capacitor, C_r	0.25 (μF)
Output filter inductor, L_f	250 (mH)
Output filter capacitor, C_f	10 (μF)

Table 2: Specifications of operating point and control parameters.

Low-voltage DC, V_{LVDC}	4.04 (kV_{DC})
Medium-voltage DC, V_{MVDC}	100.0 (kV_{DC})
Switching frequency, f_s	800 (Hz)
Rated output power, P_{out}	8.2 (MW)
Crossover frequency	15.91 (Hz)
Gain, K	58.6 (dB)
ω_p	−400 (rad/s)

infinite (>0 dB) and the phase margin Φ_M is around 78.7 deg. at 49.8 rad/s which represents that the controller is stable. The design criterion has been implemented to select the parameters for the different operation points (different output powers of the DC wind turbine), which have enough gain margin and the phase margin to deal with the parameter uncertainty and variation.

4. Modelling of DC Wind Turbine Converter for Harmonic Susceptibility Study

To identify the harmonic model of the DC wind turbine converter for the harmonic susceptibility study, the voltage harmonics within the MVDC network are considered as a perturbation on the steady-state operation point. According to the control block diagram of the SRC# given in Figure 7, the harmonic components (disturbance component $\tilde{I}_{turb}$) on the output current are dominated by the disturbance on the power reference signal P_{REF}, the disturbance in the low-voltage DC network V_g, and the disturbance in the output terminal voltage of diode rectifier V_{turb}.

Without the disturbance component in the power reference signal P_{REF} and in the low voltage DC network V_g ($\tilde{P}_{REF} = 0$ and $\tilde{V}_g = 0$), therefore, the harmonic model of WTG (wind turbine generator) considering the output LC filter (L_f and C_f) can be represented by an admittance equivalent Y_{eq} in (6) as given in Figure 9, where the harmonic admittance Y_{eq} is affected by the circuit parameters of DC wind turbine converter topology (plant model), the control design, and the output LC filter:

$$Y_{eq} = \frac{-\tilde{I}_{turb}}{\tilde{V}_{turb}} = \frac{sC_f - g_3(s)}{1 + s^2 L_f C_f + g_c(s) g_1(s) - sL_f g_3(s)}, \quad (6)$$

where the admittance of the converter without considering the output filter can be represented by the following equation:

$$Y_c = \frac{-\tilde{I}_{o,Rec}}{\tilde{V}_{o,Rec}} = \frac{-g_3(s)}{1 + g_c(s) \cdot g_1(s)}. \quad (7)$$

Equation (6) describes satisfactorily the variation of the converter current delivered to the grid in response to grid voltage disturbances where the transfer functions g_1 and g_3 in (6) and (7) (the details of expression is in (3)) describe how the output current $\tilde{I}_{o,Rec}$ is influenced by the disturbances in the control input signal $\tilde{f}_s$ and the output voltage $\tilde{V}_o$ ($\propto$ voltage V_{MVDC}), respectively. In practical applications, the output LC filter contains a tiny amount of the parasitic resistances which can alleviate the peak value of admittance magnitude Y_{eq} at the resonances frequency, as done in the following sections for the study case described in Section 6.

Figure 10(a) shows the variation of admittance magnitude $|Y_{eq}|$ of the converter with/without the output LC filter. It also represents the magnitude $|Y_c|$ of the converter without the output LC filter to observe the filter's influence on the equivalent admittance of the converter. Admittance magnitude of the converter with the output filter is high as it approaches the natural frequency of the output LC filter ($f_f \approx$ 100 Hz), while the magnitude of admittance of the converter itself (without output filter) is low in the whole spectrum and reaches a constant value at low frequencies. Regarding the phase angle of the admittance equivalent, the behavior of the converter with output filter changes from inductive, at low frequencies, to capacitive, at the natural frequency of the filter as shown in Figure 10(b).

5. Harmonic Susceptibility Study of DC Collection Network

In this section, the harmonic susceptibility study of DC collection network is revealed based on the harmonic model of the turbine converter developed previously and compared

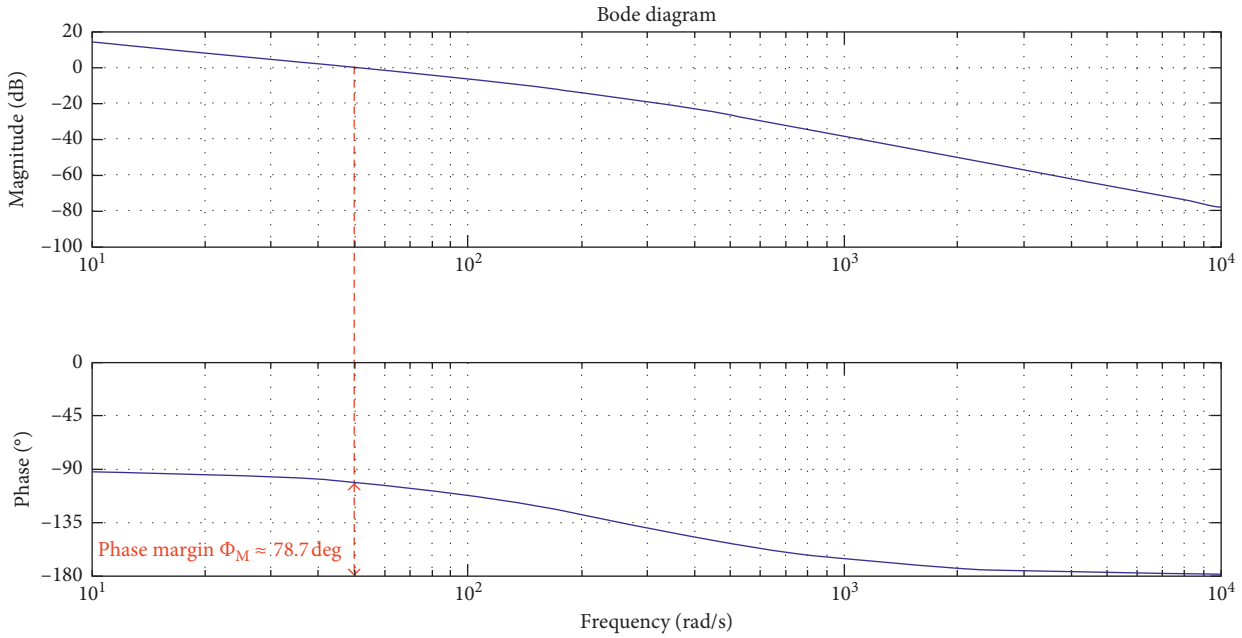

FIGURE 8: Bode plot of $g_c(s)$.

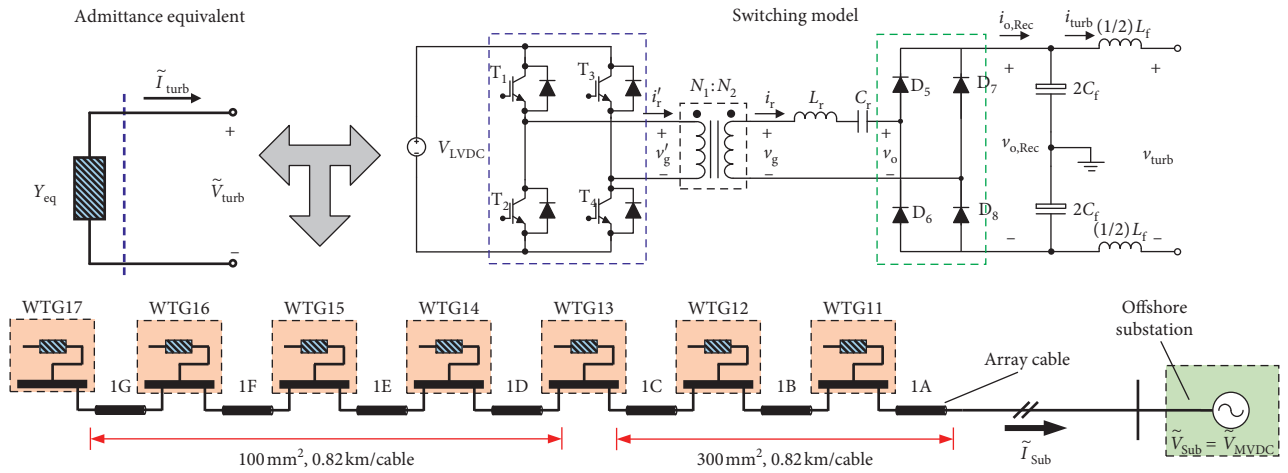

FIGURE 9: Study case of DC collection network for one single cluster of wind turbines with the proposed harmonic model (admittance equivalent) of series resonant converter SRC# (DC wind turbine generator, WTG) with the output filter included (L_f and C_f) for the harmonic susceptibility study.

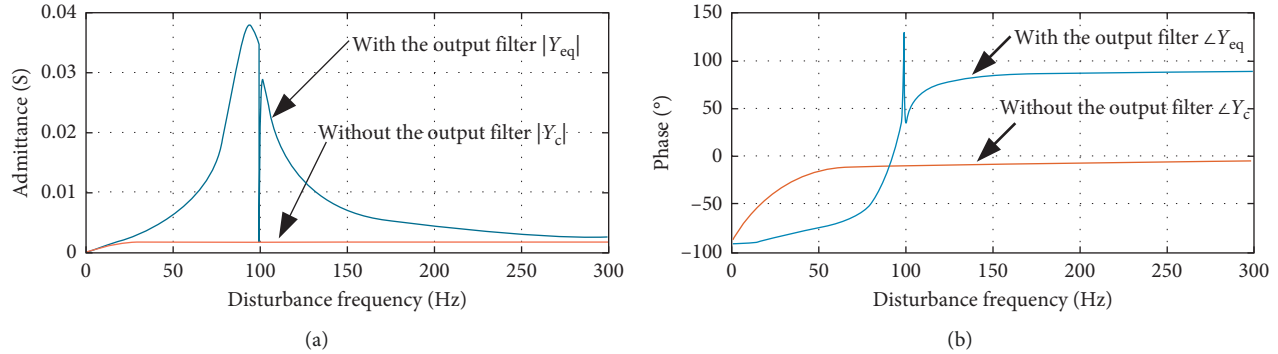

(a) (b)

FIGURE 10: Characteristic of equivalent admittance (harmonic model) of the converter for the study case of Tables 1 and 2. (a) Magnitude of admittance. (b) Phase angle of admittance.

to a switching model implemented in PLECS™. According to Figure 9, a radial-type cluster of seven wind turbines of an offshore wind power plant (OWPP) is given. It will represent the study case for the comparison of the harmonic model and switching model. The parameters for the turbine converter and operating point of the plant model with controller are given in Section 6. Since different configurations of collection network and wind turbine converter topologies could generate different harmonic spectra, background harmonics of the DC grid (correction/array network) from the offshore substation DC/DC converter and DC wind turbine generator (DC WTG) can cause undesirable resonant phenomena and raise stability issues. One of the major tasks of the harmonic susceptibility study is to identify resonance frequencies of network and investigate potential voltage amplification issues.

5.1. Cable Model. Array cables in the following study cases are modelled as a pi-equivalent model with longitudinal admittance parallel branches in order to consider the frequency dependency of distributed cable parameters and represent correctly the behavior in the frequency ranging from 0 to 10 kHz [31, 44]. In the study, the electromagnetic transient program *PSCAD* is usefully employed to extract the longitudinal admittance and the shunt capacitance from the geometric data of array cable [41]. The values of resistance, inductance, and capacitance to use at each frequency are calculated by the software individually.

According to the cable model in *PSCAD*, the capacitance is not varying within the range of interesting frequency. Instead, as the frequency rises, the resistance keeps increasing, due to the skin effect, and the inductance decreases its value due to the eddy currents in the outer conductors. For the considered study case, eight *RL* series branches are used to approximate the longitudinal impedance.

The *PSCAD* generates the admittance date (i.e., matrix $[Z_{\mathrm{PSCAD}}]$ and $[Y_{\mathrm{PSCAD}}]$) from the geometrical data of the marine cable (in frequency-dependent (phase) model) in certain operational frequency to form "pi-equivalent cable model" [45]. An equivalent pi-equivalent model is built based on the cable model, which can fit the admittance date (matrix $[Z_{\mathrm{PSCAD}}]$ and $[Y_{\mathrm{PSCAD}}]$) from the geometrical data of the submarine cable (implemented in frequency-dependent (phase) model in *PSCAD*) to make sure that the adequate cable model is implemented in the array cable network. Actually, the frequency-dependent phase model in *PSCAD* is also regarded as a most numerically accurate cable model thus far. The formulation of models has been proved that the bandwidths of the model can be up to 1 MHz, which can satisfy most of transient studies and harmonics studies [41, 45].

5.2. Frequency Scan Approach. The WPP cluster consists of seven turbines with seven MVDC cable segments, where the offshore substation converter is represented by an ideal harmonic voltage source. According to the frequency scan approach for network analysis addressed in Figure 11, the harmonic voltage source (disturbance component) in the output DC voltage of the offshore substation converter is activated and injects harmonic voltage component into the MVDC grid with 0.5% (=0.005 p.u) of voltage magnitude ($|V_{\mathrm{MVDC,h,n}}| = 500$ V) and the frequency of injected harmonic voltage raises until 300 Hz, by steps of 20 Hz. The output voltage and output current traces of each wind turbine model in each frequency step are extracted for *FFT* analysis after the steady-state condition is reached. This approach allows an arbitrary choice of frequency and magnitude of the disturbance in the offshore substation. Therefore, it does not intend to represent only a specific range of harmonics in the DC collection network. Eventually, models of the DC collection system (or network) could be established for different frequencies of the injected disturbances. As an example, for the harmonic model, the wind turbine converter can be described by a particular *RL* or *RC* series branch for disturbance frequency.

Based on the harmonic model of DC collection network in Figure 9, Figure 11 gives a flow chart of frequency scan approach for the DC collection system in the harmonic susceptibility study. The process includes the identification of the harmonic model of the DC wind turbine for certain frequency of the injected disturbance (harmonic) and the establishment of the harmonic model of DC collection network. The DC collection network in Figure 9 is set as an example to explain the sequence of frequency scan illustrated in Figure 11. *Step 1*: the harmonic voltage source in the offshore substation ($\widetilde{V}_{\mathrm{MVDC}}$) is connected to the network and injects a 20 Hz harmonic disturbance into the MVDC network with a specific voltage magnitude $|V_{\mathrm{MVDC}}|$. The harmonic model of the DC wind turbine generator (WTG) under 20 Hz perturbation (harmonic frequency) in MVDC network is identified by connecting to the MVDC network at $t = t_1$. *Step 2*: the voltage and current within network are extracted for *FFT* analysis after the voltage and current have reached the steady-state condition. *Step 3*: at $t = t_2$, the frequency for which the harmonic model of the DC wind turbine is evaluated and is increased by 20 Hz, as the frequency of the injected disturbance. The algorithm turns back to *Step 2*. Eventually, the frequency sweep continues until 300 Hz (at $t = t_{n-1}$), which depends on the control bandwidth of the DC wind turbine converter and interesting frequency range in the harmonic susceptibility study.

6. Verification

Based on the DC collection network in Figure 9 and the converter control design addressed in (5), Tables 1 and 2 give the parameters used in the study of the DC collection grid, where the geometric parameters of cables are shown in Figure 12 which is implemented in the created equivalent PI section according to the frequency-dependent (phase) model in *PSCAD*. For the turbine harmonic model, all the turbines are considered operating in the same operating point, described in Table 2. As far for the switching model, wind turbine converters are operated with a switching frequency of 800 Hz that guarantees around an output power of 8.2 MW when the output voltage of the converter is 100 kV. The LVDC source (input voltage) of each converter

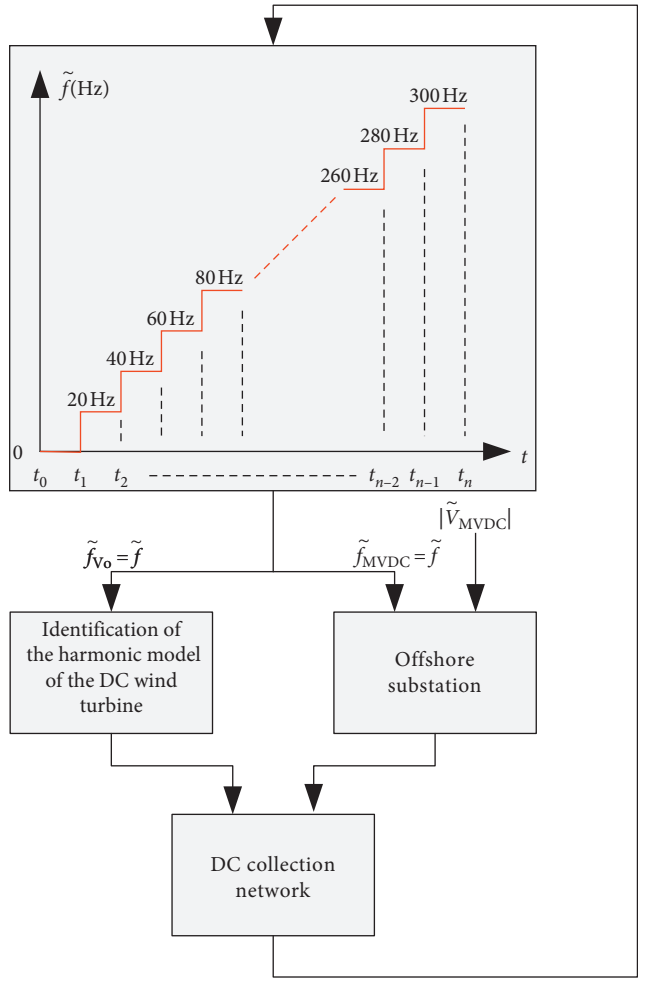

Figure 11: Frequency scan approach in the harmonic susceptibility study.

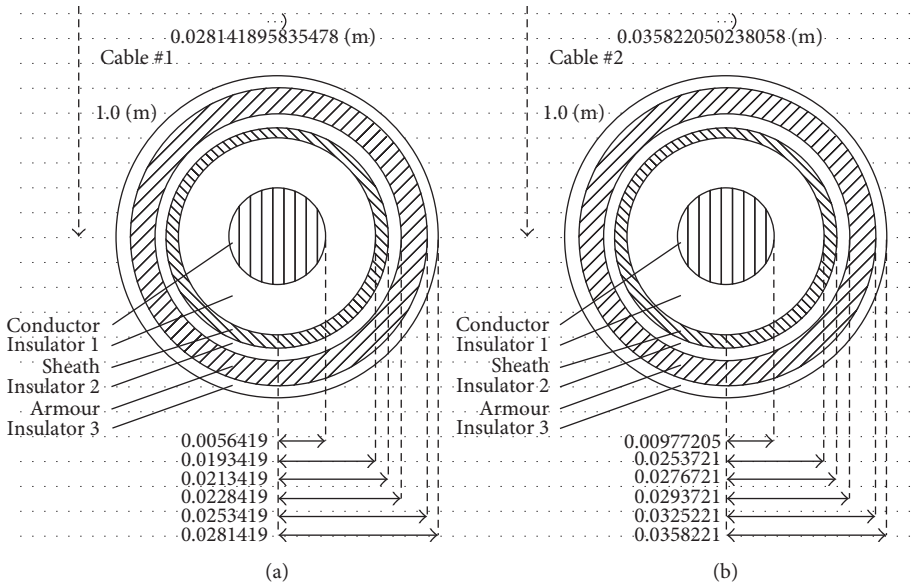

Figure 12: MVDC submarine array cables spacing and dimensions (XLPE, pairs of single core conductor cross section 100 mm^2 (a) and 300 mm^2 (b)) [41].

is 4.04 kV, while the voltage drops across cables are responsible for different voltages at the output terminal of the wind turbines. The controller of each turbine regulates the switching frequency in order to control the output power to follow its reference. In particular, the frequencies are higher as wind turbines move further away from the offshore substation, to compensate the lower voltage difference on the two sides of the converter. According to the frequency scan approach illustrated in Figure 11, additionally, a perturbation with a specific sequence of frequency in the range of 20 to 300 Hz is applied to the corresponding harmonic model of turbine converter and the results are given in Figure 13 for a single wind turbine.

Figure 13 gives a verification of the turbine harmonic model (equivalent admittance) by comparing the harmonic spectrum of output current with the results generated by the corresponding switching model of the turbine converter in PLECS™. The current spectrum shows that the derived harmonic model and converter switching model are very close up to 300 Hz. The magnitude of output current spectrum is reduced as the frequency of the harmonic component is far from the natural frequency of the output LC filter, where the mismatch between the harmonic model and its switching model in PLECS™ becomes higher. Furthermore, the turbine output current trace shows that the harmonic component of output current is amplified, while the frequency of MVDC harmonic voltage ($V_{\mathrm{MVDC,h,n}}$) approaches to the natural frequency of output LC filter of the turbine converter.

The results of network (array network) simulation in Figure 14 between both models (harmonic model and the corresponding switching model) show a good agreement. However, some mismatch coming from the harmonic model developed can be seen in all turbines in cluster. Furthermore, as observed along the cluster, last wind turbines (shown in Figures 14(f) and 14(g)) have second- and third-order current harmonics due to nonlinear behavior considered by the turbine converter switching model. This is because the proposed harmonic model cannot predict these higher order harmonics since the modelling approach for the turbine converter in MVDC network are linear. Figure 15 gives a comparison of the harmonic spectrum of output current for wind turbines at different locations to study the error of the harmonic model. While in the closest WTG to the offshore substation, a sinusoidal wave is observed (WTG11); in the last ones, sinusoidal waves have a considerable amount of harmonic components at multiples of the injected disturbance frequency (WTG17). Furthermore, the amplitudes of the fundamental current harmonics decrease along the cluster, approaching the farthest wind turbine from the offshore substation. This phenomenon is related to the rising amplitude of higher order harmonics as depicted in Figure 15. Additionally, it is worth mentioning that, in the switching model, there are current harmonics around 1600 Hz, twice of the switching frequency of converter, as the filter at the output of each converter cannot cancel completely these current harmonics.

The harmonic current spectrum at natural frequency of the output LC filter (≈100 Hz) was not shown in the grid simulation in Figure 14 because it was in the equivalent turbine model (admittance equivalent), since it was "ideal" current source (linear model), the parameters were really high and were not matching the switching model at al. Probably the filter damping is too small which results in very high current (approx. 500 A) at resonance of the output LC filter for a single turbine in grid simulation (equivalent model). However, the results of grid simulation still shows that the admittance equivalent follows results from the switching model for a single turbine in all frequencies; at natural frequency of the turbine output LC filter, the admittance equivalent is clearly not well represented.

In the verification of modelling of the array cable with equivalent PI-cable section based on the method proposed by Beerten et al. [31], the values of resistance and inductance of each branch are calculated in order to fit the behavior of the longitudinal admittance in the frequency domain calculated by *PSCAD's cable model* (frequency-dependent (phase) model). Figure 16 shows a good matching of the fitted values of the admittance by the eight parallel branches ($N = 8$) and the values calculated by software (*PSCAD's cable*). The error on the magnitude of the admittance between two models is less than 1.0%, within the range of 0.001 Hz–10000 Hz. The error in phase is always less than 1.7°, in the range of interesting frequency.

Since the calculation of the admittance date from the frequency-dependent (phase) model in *PSCAD* is not straightforward and is extremely complicate, there are some articles which are useful to conduct the calculation of admittance date from the geometry date of the cable model [28, 30, 45].

7. Laboratory Test

A laboratory test is performed to prove the validity of the proposed harmonic model of the turbine converter. A schematic of the setup of the DC wind turbine converter for SRC# is depicted in Figure 17. The down-scale prototype circuit with 216 $\mathrm{V_{DC}}$ (V_{LVDC}) to 400 $\mathrm{V_{DC}}$ (V_{MVDC}) DC wind turbine converter is built to verify the harmonic distribution of the turbine converter. The wind turbine converters, whatever AC or DC turbines, are the boost structures in order to increase the efficiency of power transmission. Therefore, the down-scale prototype circuit is designed to match with this character (boost the low-voltage DC, V_{LVDC}, from the generator) to match with the DC grid voltage (medium-voltage DC, V_{MVDC}) from the offshore substation. Although only a single turbine converter is implemented in the test bench, the harmonic signatures of the wind turbine converter (in the test bench) in the interesting frequency range have been confirmed which match with the simulation model as in the following results.

A programmable AC source is used to emulate the harmonic voltage source ($V_{\mathrm{MVDC,h}}$) with sinusoidal waves at different frequencies on the output terminal of the converter. A module of resistors R_{load} and a diode D_{Aux} are placed on the output side of the converter to simulate the character of unidirectional power flow of MVDC network. Table 3

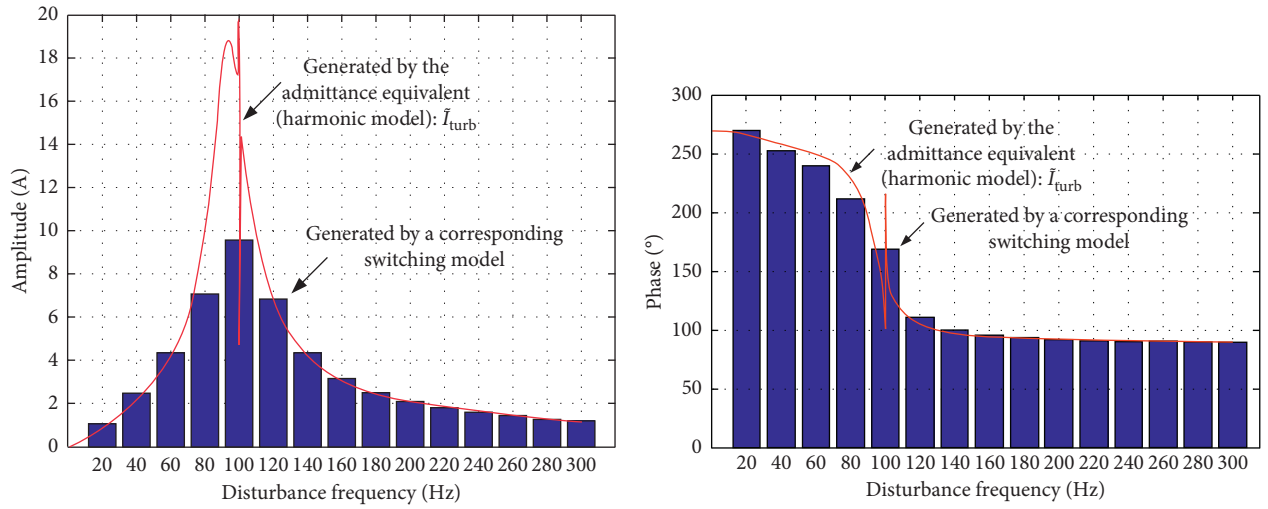

Figure 13: Spectrum of turbine output current with a 0.005 p.u harmonic disturbance on the output voltage terminal of the single wind turbine converter ($V_{MVDC} = \pm 50$ kV). (a) Magnitude of current harmonic. (b) Phase angle of current harmonic.

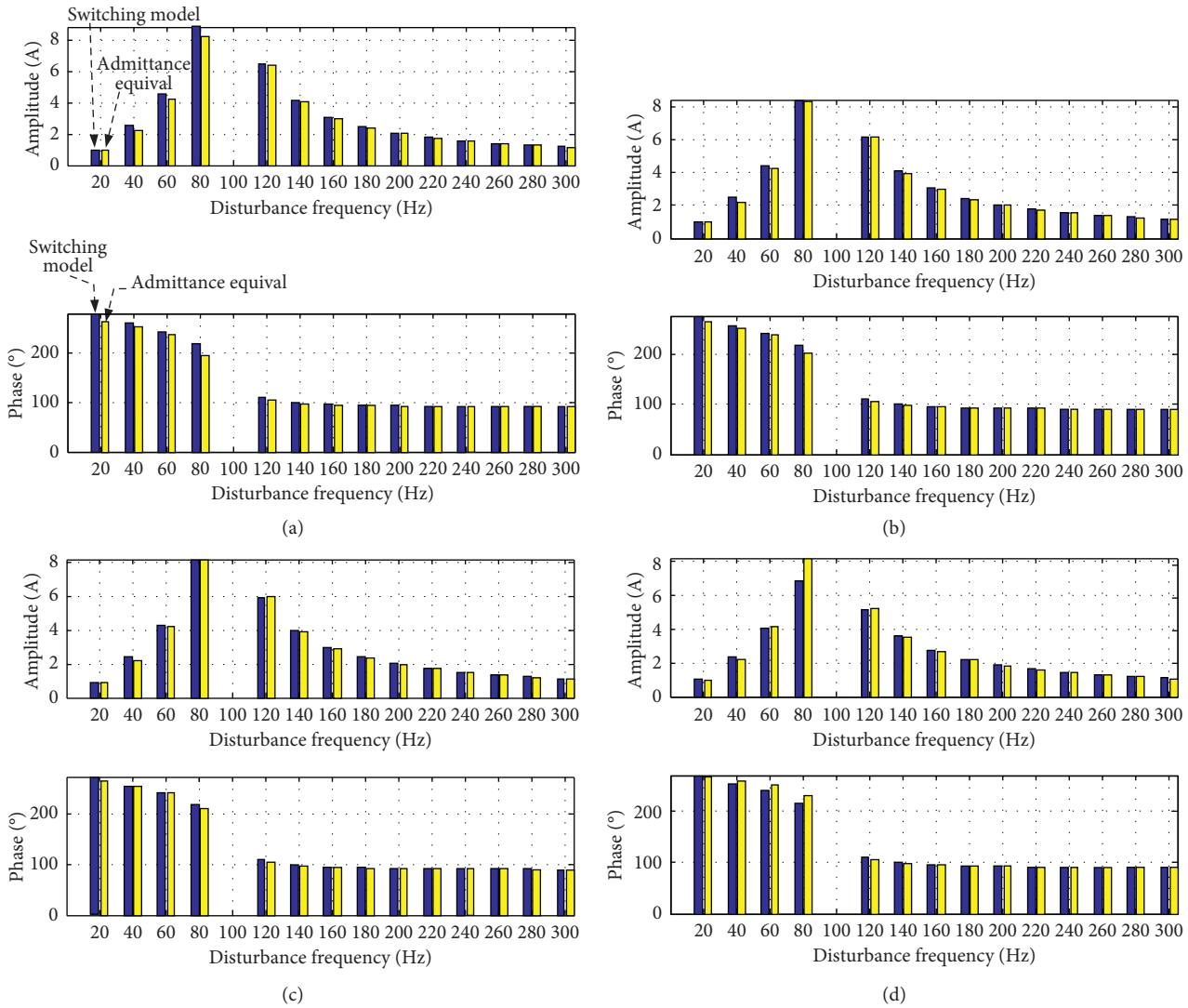

Figure 14: Continued.

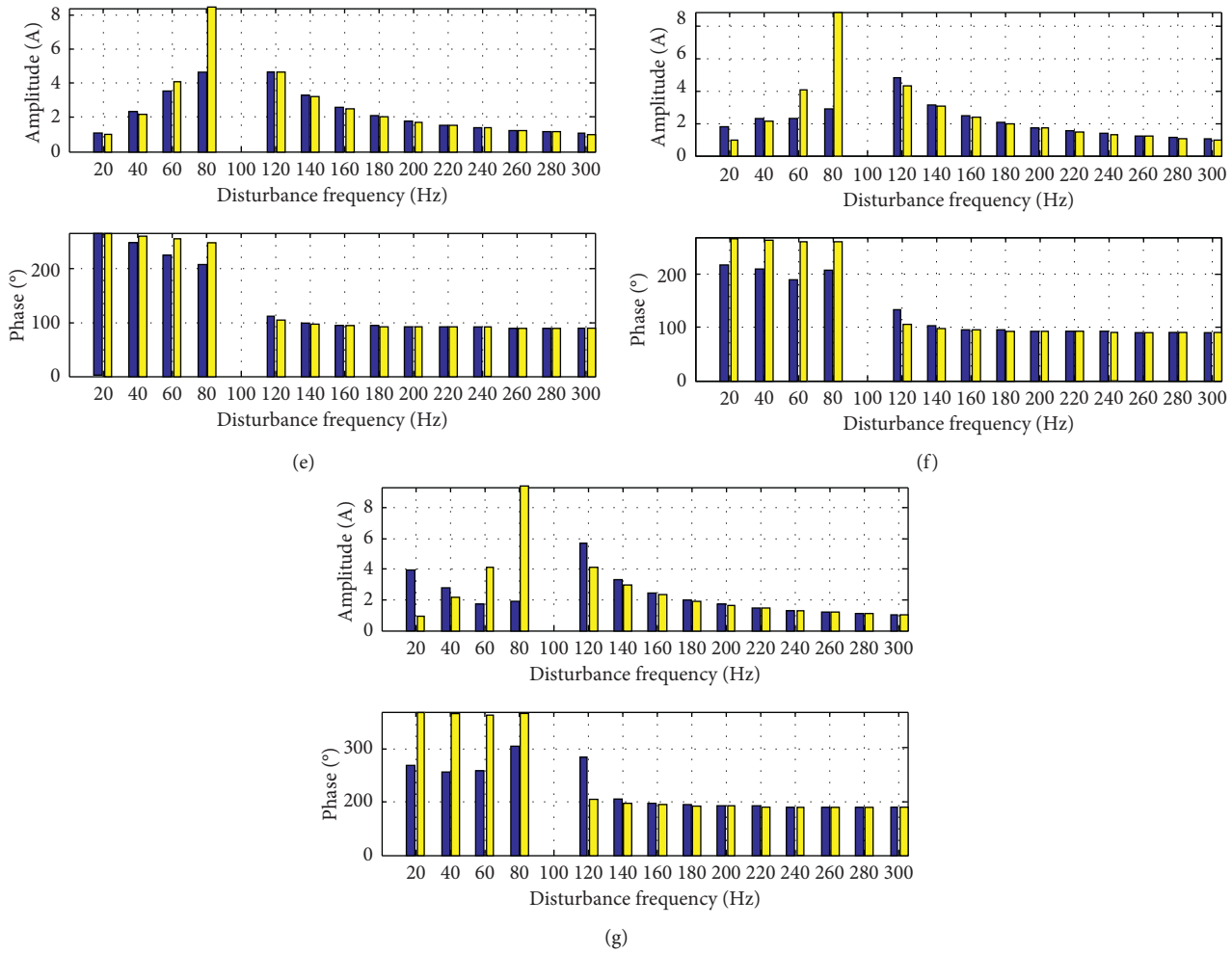

Figure 14: Output current spectrum of individual turbines in the operating point described in Tables 1 and 2, being WTG11 the closest to the offshore substation and WTG17 the furthest. Harmonic current amplitude and phase angle are represented for a switching model of the DC wind turbine converter ($|I_{\text{turb,sw,WTGxx}}|\angle\theta_{\text{turb,sw,WTGxx}}$) and for the admittance equivalent model (harmonic model) ($|I_{\text{turb,eq,WTGxx}}|\angle\theta_{\text{turb,eq,WTGxx}}$). (a) WTG11. (b) WTG12. (c) WTG13. (d) WTG14. (e) WTG15. (f) WTG16. (g) WTG17.

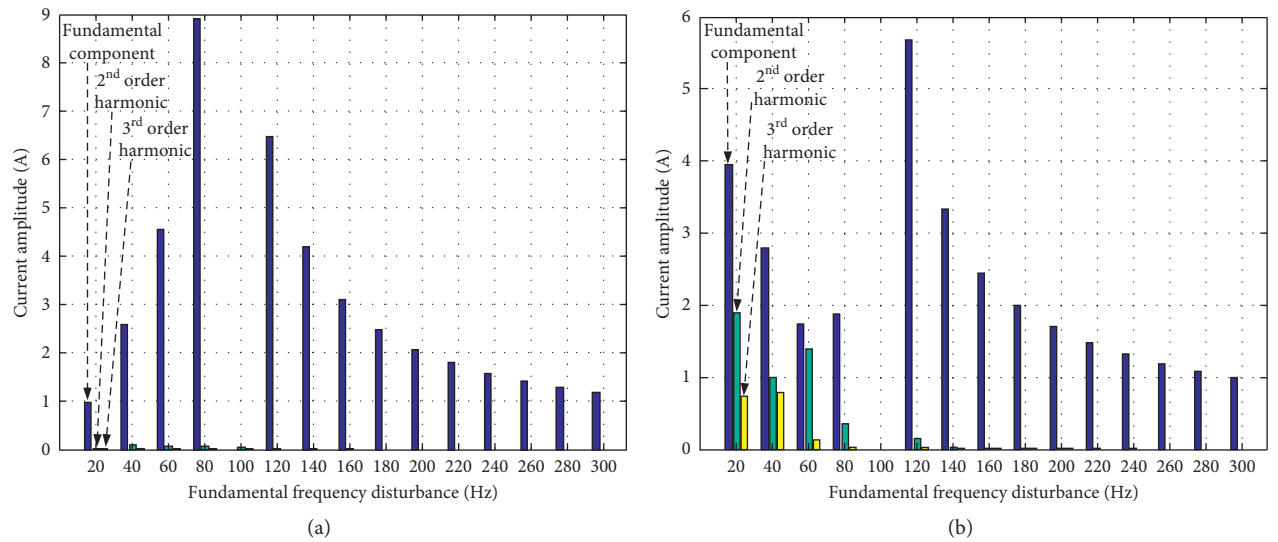

Figure 15: A comparison of output current magnitudes for the switching model in PLECS™ for the WTG11 (first WTG) (a) and WTG17 (seventh WTG) (b) (fundamental component: injected harmonic component).

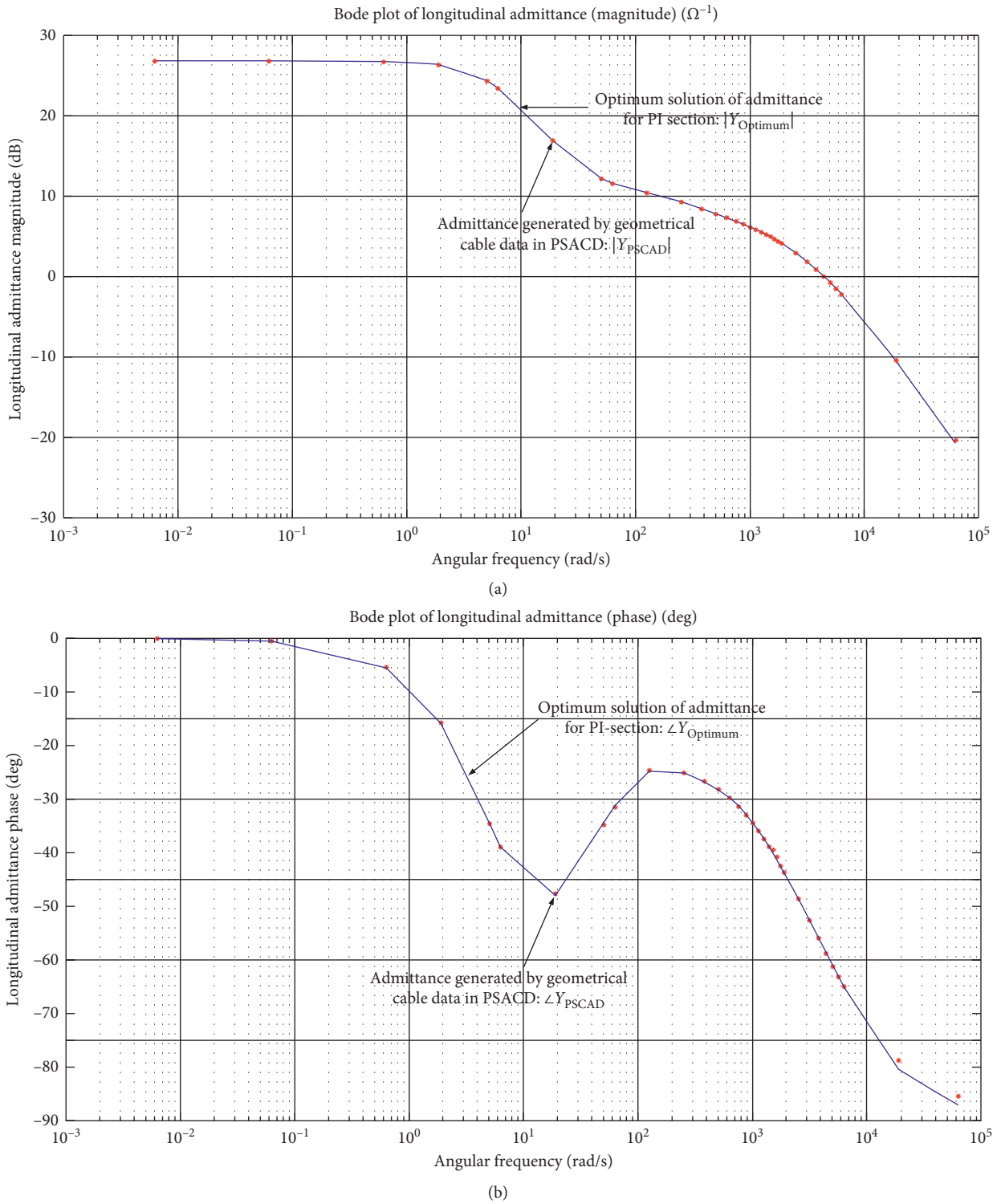

FIGURE 16: Results of the optimum vector fitting for the longitudinal admittance of the submarine array cable with the parallel of *eight* RL series branches. The longitudinal admittance values found in *PSCAD* are highlighted in red star (points), while the admittance of the parallel of the *eight* series RL branches is depicted in blue curve (line). (a) Magnitude of calculated admittance. (b) Phase angle of calculated admittance.

describes the power rating and circuit parameters of the laboratory test bench of *SRC#* where the average of *output voltage* is around 400 V_{DC} ($V_{MVDC} = V_{turb}$, DC component of output voltage of the turbine) and the *output current* (DC component of output current of the turbine) is around 1.4 A_{DC}.

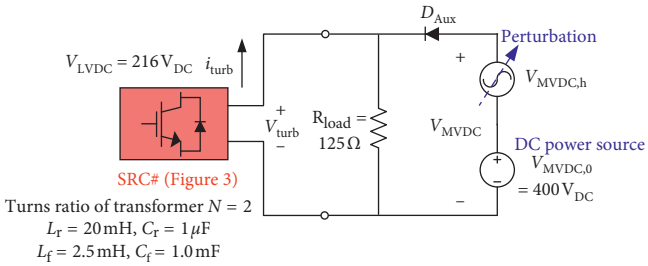

Figure 17: Schematic of the laboratory setup for experiment.

Table 3: Specifications of the laboratory test bench.

Low-voltage DC source, V_{LVDC}	216 (V_{DC})
DC component of medium-voltage source, $V_{MVDC,0}$	400 (V_{DC})
Transformer winding voltage ratio, $N_1 : N_2$	1 : 2
Output power, P_{out}	550 (W)
Resonant inductor, L_r	20.0 (mH)
Resonant capacitor, C_r	1.0 (μF)
Output filter inductor, L_f	2.5 (mH)
Output filter capacitor, C_f	1.0 (mF)
Resistive load, R_{load}	125 (Ω)
Duty cycle	50%

A harmonic model and switching model in PLECS™ are also developed with the parameters of the laboratory setup for the comparison. The operating switching of SRC# is set to 800 Hz with 50% duty cycle and an output power of 550 W. Input voltage (V_{LVDC}) is set to 216 V, which is 11 V slightly higher than the input voltage (205 V) in the switching model developed in PLECS™ to take into account voltage drops in the practical setup. The DC component of converter's output voltage ($V_{MVDC,0}$) is set to 400 V. A harmonic voltage source ($V_{MVDC,h}$) of $3.5V_{RMS}$, with frequency varying in the range of 20 to 300 Hz, is used for harmonic susceptibility tests. Harmonics current in the output are recorded and the results from the laboratory experiment, PLECS™ simulations, and the admittance equivalent developed for the laboratory setup are compared in Figure 18. The results show that there is a good agreement with the proposed DC turbine harmonic model. However, there is a mismatch in the amplitudes (Figure 18(a)) when the injected frequencies approach the natural frequency of the output LC filter. As given in Section 4, the admittance of the DC turbine harmonic model is heavily influenced by the output LC filter. The behavior of the converter changes from inductive to capacitive at the natural frequency of the filter as in Figure 18(b).

It should be noted that there is no standard for selecting the medium-voltage DC (MVDC) grid. The MVDC of 400 V_{DC} is chosen as output voltage of the down-scale prototype circuit of SRC# from the available test equipment in the laboratory for simulating the MVDC gird (controllable DC power source). In practical applications, the selection of MVDC is based on the electromagnetic transient (EMT) simulation of the grid and existing offshore wind farm technologies such as power converters, protection devices, available offshore platform, and array cables [1].

8. Conclusion

A model-based methodology in conducting the harmonic susceptibility study is revealed based on the discrete time-domain modelling technique and the frequency scan approach in the frequency domain. The developed harmonic model in the paper can be used to perform a harmonic susceptibility study of power collection network in an early stage of a wind farm project because of its simplicity and low computational cost compared to a switching model. In the later stage, the proposed method is recommended to consider the switching model of the converters in order to be closer to reality. The process of harmonic susceptibility study contains identification of the harmonic model of the turbine converter and the establishment of array network in the frequency domain. The validation of the harmonic model of the turbine converter is given in Sections 6 and 7 via computer simulation implemented in PLECS™ and the laboratory tests, respectively. Additionally, the distribution of current harmonics within DC collection network is investigated including the identification of possible resonance frequency within array network. Moreover, analytical data from simulation and the laboratory tests give indications to set a proper design and natural frequency for the output LC filter of the DC turbine converter and a matched switching frequency for the converter placed in the offshore substation.

Appendix

According to the flow chart of mathematical derivation in Figure 6 in Section 3, firstly, the circuit topology of the turbine converter and mode of operations are decided as shown in Figures 3 and 19, and then the equivalent circuit based on the switching sequence of transistors is created as shown in Figure 20. In Figure 20, the large-signal model of the converter is generated (Step 4) and then the interesting state variables (Step 5) are defined to create the small-signal equations. Steps 6 and 7 establish the space model of the plant. Finally, the converter plant mode is established based on the *discrete time-domain modelling* approach proposed in (Step 8) [42, 46]. Step 9 gives a set of interesting transfer function of the output LC filter. Eventually, Steps 10 to 12 focus on the control design for SRC#.

A. Derivation of the Plant Model

Steps 1–3. Decide the circuit topology of DC turbine converter, resonant tank waveform, and equivalent circuit.

Steps 1–3 describe how to obtain the large-signal model and the corresponding equivalent circuit in subresonant CCM in Figure 20 from the circuit topology of SRC#, which is operated in subresonant CCM as in Figures 3 and 20, respectively. The waveform in Figure 19 is divided by different time zones (different switching sequences) based on the *discrete time-domain modelling* approach. The figures are eventually used to generate the large-signal model of SRC#.

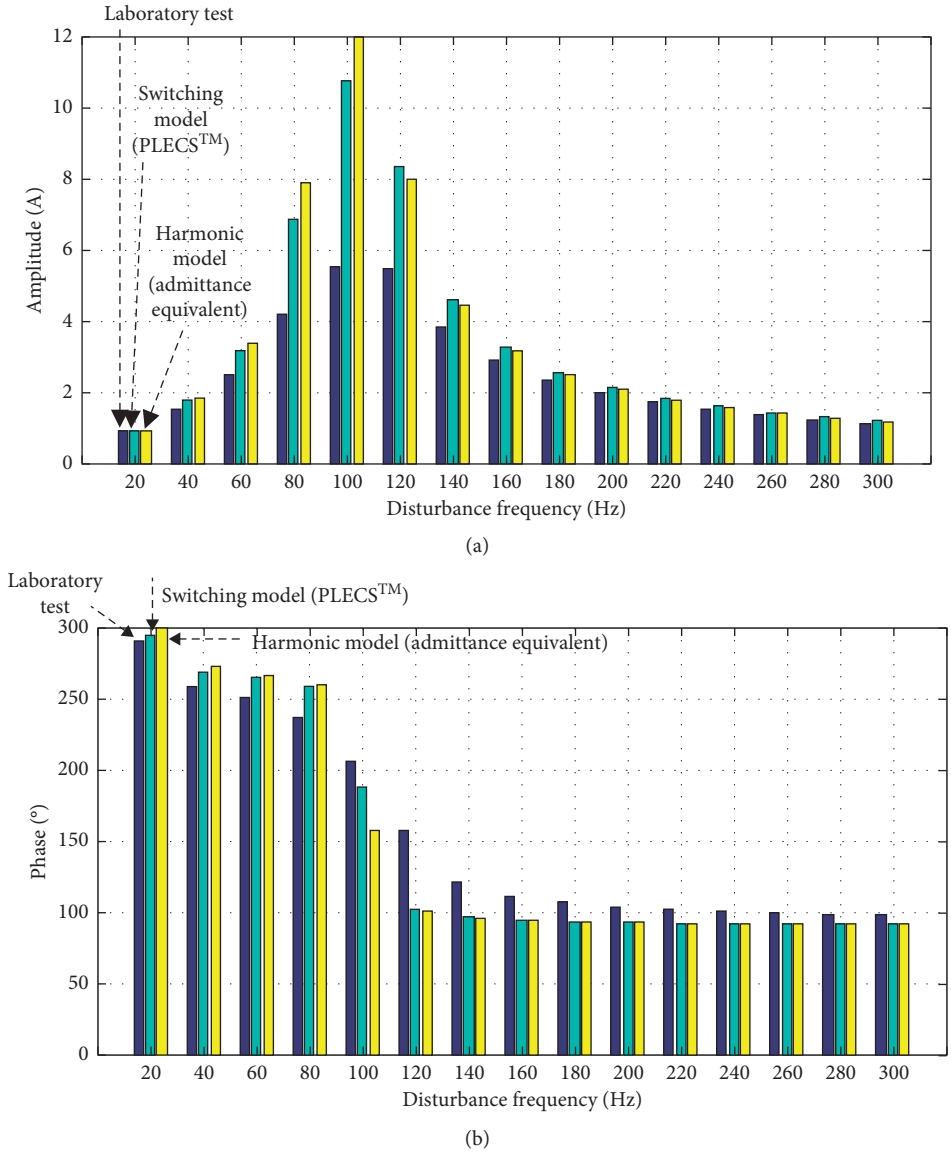

FIGURE 18: Harmonic spectrum of output currents for the scaled-down experiment, with 5.0 V perturbation in amplitude in the range of 20 to 300 Hz: laboratory test result, result generated by the switching model in PLECS™ simulation and result generated by the proposed harmonic model. (a) Magnitude of current harmonics. (b) Phase angle of current harmonics.

Step 4. Large-signal model.

In the large-signal model, the final value of interesting state variables in each switching interval is represented by the initial values of states. According to *discrete time-domain modelling* approach, the procedure is only valid when the variations in MVDC grid voltage $v_o(t)$ (output terminal voltage) and LVDC voltage $v_g(t)$ (input terminal voltage) in the event (switching) are relatively small than their initial and final values [42]. According to Figures 19 and 20, Equations (A.1), (A.3), (A.4), (A.6)–(A.10), (A.12), and (A.13) show the details of derivation of the large-signal model of resonant inductor current $i_r(t)$, capacitor voltage $v_{Cr}(t)$, and their end values at k_{th} event in terms of initial values of k_{th} event.

For $t_{0(k)} \le t \le t_{1(k)}$ (T_1, T_4 ON),

$$v_g = L_r \frac{di_r}{dt} + v_{Cr} + v_o,$$
$$i_r = C_r \frac{dv_{Cr}}{dt}, \tag{A.1}$$

where

$$v_g = V_{g,0(k)},$$
$$v_o = V_{o,0(k)}. \tag{A.2}$$

The resonant inductor current $i_r(t)$ and resonant capacitor voltage $v_{Cr}(t)$ can be obtained by (A.1):

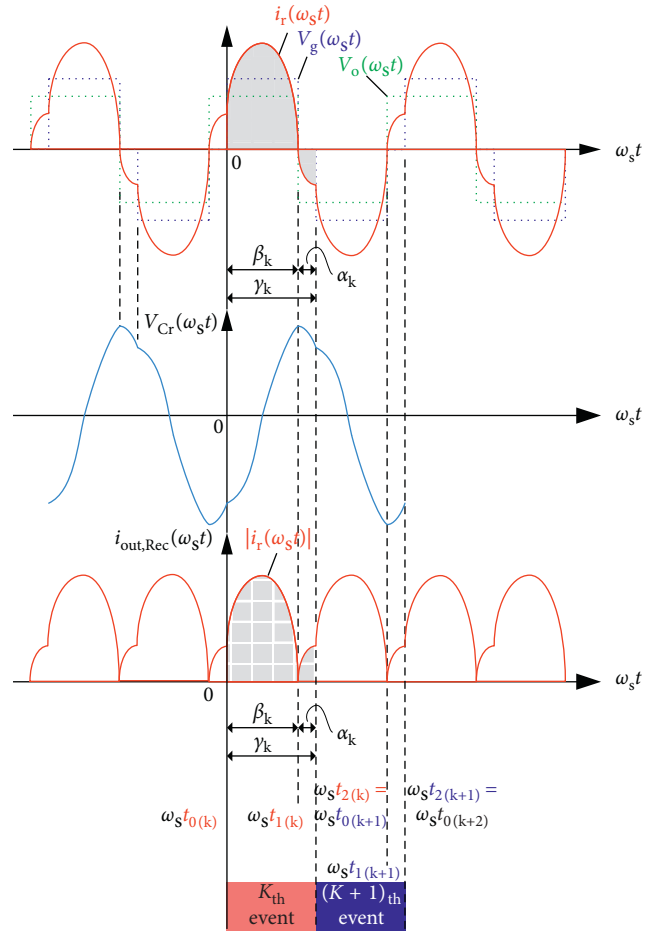

Figure 19: Resonant inductor current and resonant capacitor voltage waveforms of SRC# in subresonant CCM.

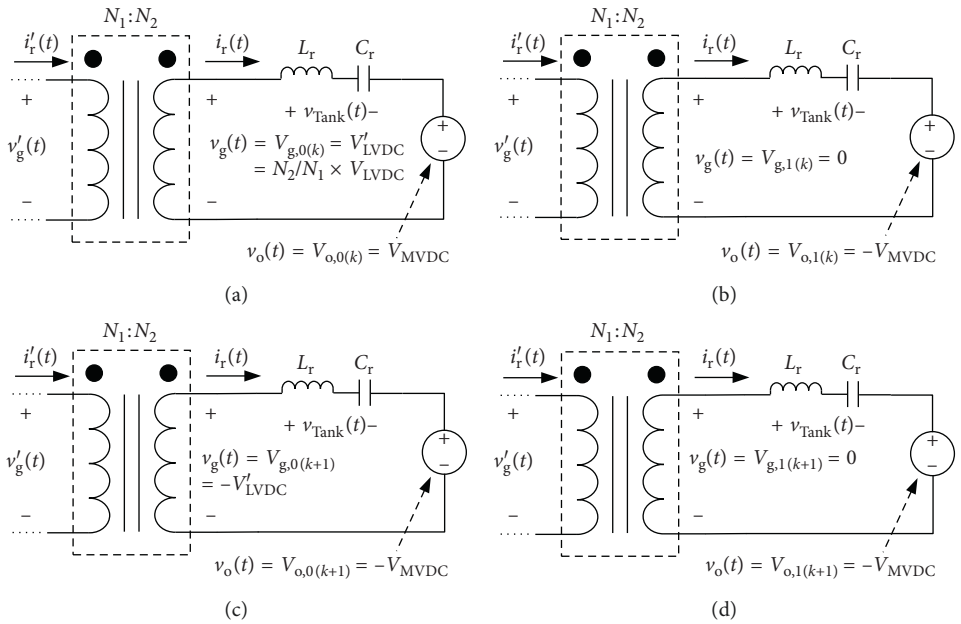

Figure 20: Equivalent circuit of SRC# for large-signal analysis of conduction intervals in subresonant CCM. (a) $t_{0(k)} \le t \le t_{1(k)}$ (T_1, T_4 ON). (b) $t_{1(k)} \le t \le t_{2(k)}$ (D_1, T_3 ON). (c) $t_{0(k+1)} \le t \le t_{1(k+1)}$ (T_2, T_3 ON). (d) $t_{1(k+1)} \le t \le t_{2(k+1)}$ (D_2, T_4 ON).

$$i_r = \frac{1}{Z_r}\left(V_{g,0(k)} - V_{o,0(k)} - V_{Cr,0(k)}\right)\sin\left(\omega_r t\right) + I_{r,0(k)}\cos\left(\omega_r t\right), \tag{A.3}$$

$$v_{Cr} = V_{g,0(k)} - \left(V_{g,0(k)} - V_{o,0(k)} - V_{Cr,0(k)}\right)\cos\left(\omega_r t\right) + I_{r,0(k)} Z_r \sin\left(\omega_r t\right) - V_{o,0(k)}, \tag{A.4}$$

where

$$Z_r = \sqrt{\frac{L_r}{C_r}}, \qquad \omega_r = \frac{1}{\sqrt{L_r C_r}}. \tag{A.5}$$

At time $t = t_{1(k)}$, the tank current i_r reaches the point of zero crossing, commutating the IGBT switches T_1 and T_4 turnoff and turning on body-diode D_1, and IGBT switch T_3. Therefore, the resonant inductor current $i_r(t)$ can be expressed by

$$I_{r,1(k)} = i_r\left(t_{1(k)}\right) = \frac{1}{Z_r}\left(V_{g,0(k)} - V_{o,0(k)} - V_{Cr,0(k)}\right)\sin\left(\omega_r t_{1(k)}\right) + I_{r,0(k)}\cos\left(\omega_r t_{1(k)}\right) = 0, \tag{A.6}$$

where

$$\omega_r t_{1(k)} = \frac{\omega_r}{\omega_s}\beta_K = \omega_{rs}\cdot\beta_K \quad \text{for } t_{0(k)} = 0, \qquad \tan\left(\omega_{rs}\beta_K\right) = \frac{-I_{r,0(k)} Z_r}{\left(V_{g,0(k)} - V_{o,0(k)} - V_{Cr,0(k)}\right)}, \tag{A.7}$$

$$0 < \left(\omega_{rs}\beta_K\right) \le \pi, \quad t_{1(k)} = \beta_K/\omega_s,$$
$$V_{Cr,1(k)} = v_{Cr}\left(t_{1(k)}\right) = V_{g,0(k)} - \left(V_{g,0(k)} - V_{o,0(k)} - V_{Cr,0(k)}\right)\cdot\cos\left(\omega_{rs}\beta_K\right) + I_{r,0(k)} Z_r \cdot \sin\left(\omega_{rs}\beta_K\right) - V_{o,0(k)}. \tag{A.8}$$

For $t_{1(k)} \le t \le t_{2(k)}$ (D_1, T_3 ON),

$$i_r\left(t'\right) = \frac{-1}{Z_r}\left(V_{o,1(k)} + V_{Cr,1(k)}\right)\sin\left(\omega_r t'\right), \tag{A.9}$$

where

$$t' = t - t_{1(k)}, \qquad v_{Cr}\left(t'\right) = \left(V_{o,1(k)} + V_{Cr,1(k)}\right)\cos\left(\omega_r t'\right) - V_{o,1(k)}, \tag{A.10}$$

where

$$I_{r,1(k)} = 0, \qquad V_{g,1(k)} = 0, \qquad V_{o,1(k)} = -V_{MVDC} = -V_{o,0(k)}. \tag{A.11}$$

Eventually, the end values of inductor current $i_r(t)$ and capacitor voltage $v_{Cr}(t)$ (at time $t = t_{2(k)}$) can be written as

$$I_{r,2(k)} = \left[-\sin\left(\omega_{rs}\beta_K\right)\cdot\sin\left(\omega_{rs}\alpha_K\right)\right]\cdot I_{r,0(k)} + \left[-\frac{1}{Z_r}\cdot\cos\left(\omega_{rs}\beta_K\right)\cdot\sin\left(\omega_{rs}\alpha_K\right)\right]\cdot V_{Cr,0(k)} + \left[\frac{2}{Z_r}\cdot\sin\left(\omega_{rs}\alpha_K\right) + \frac{-1}{Z_r}\cdot\cos\left(\omega_{rs}\beta_K\right)\cdot\sin\left(\omega_{rs}\alpha_K\right)\right]\cdot V_{o,0(k)} + \left[\frac{-1}{Z_r}\cdot\sin\left(\omega_{rs}\alpha_K\right) + \frac{1}{Z_r}\cdot\cos\left(\omega_{rs}\beta_K\right)\cdot\sin\left(\omega_{rs}\alpha_K\right)\right]\cdot V_{g,0(k)}, \tag{A.12}$$

$$V_{Cr,2(k)} = \left[Z_r\cdot\sin\left(\omega_{rs}\beta_K\right)\cdot\cos\left(\omega_{rs}\alpha_K\right)\right]\cdot I_{r,0(k)} + \left[\cos\left(\omega_{rs}\beta_K\right)\cdot\cos\left(\omega_{rs}\alpha_K\right)\right]\cdot V_{Cr,0(k)} + \left[-2\cdot\cos\left(\omega_{rs}\alpha_K\right) + \cos\left(\omega_{rs}\beta_K\right)\cdot\cos\left(\omega_{rs}\alpha_K\right) + 1\right]\cdot V_{o,0(k)} + \left[\cos\left(\omega_{rs}\alpha_K\right) - \cos\left(\omega_{rs}\beta_K\right)\cdot\cos\left(\omega_{rs}\alpha_K\right)\right]\cdot V_{g,0(k)}, \tag{A.13}$$

where

$$\omega_s\cdot\left(t_{2(k)} - t_{1(k)}\right) = \alpha_K. \tag{A.14}$$

The same process of derivation as given in (A.1), (A.3), (A.4), (A.6)–(A.10), (A.12), and (A.13) can be applied for obtaining the large-signal expression of resonant inductor current $i_r(t)$ and resonant capacitor voltage $v_{Cr}(t)$ in $(k+1)_{th}$ event ($t_{0(k+1)} \le t \le t_{1(k+1)}$ and $t_{1(k+1)} \le t \le t_{2(k+1)}$).

A.1. Steady-State Solution of Large-Signal Model. The following equation expresses the conditions for obtaining steady-state solution (at certain operating points of CCM) of the discrete state equation of the large-signal model:

$$I_{r,2(k)} = -I_{r,0(k)}, \qquad V_{Cr,2(k)} = -V_{Cr,0(k)}. \tag{A.15}$$

By substituting (A.15) into (A.12) and (A.13), the steady-state solution of $I_{r,0(k)}$ and $V_{Cr,0(k)}$ can be written in term of $V_{o,0(k)}$, $V_{g,0(k)}$, β_k, and α_k:

$$\overline{I}_r = I_{r,0(k)} = f\left(V_{o,0(k)}, V_{g,0(k)}, \beta_K, \alpha_k\right), \qquad \overline{V}_{Cr} = V_{Cr,0(k)} = f\left(V_{o,0(k)}, V_{g,0(k)}, \beta_K, \alpha_k\right), \tag{A.16}$$

where the overbar used in equations is to indicate the steady-state value of the interesting state variables. For simplifying the derivation of the plant model, the output LC filter of SRC# (i.e., L_f and C_f) is neglected due to a very slow dynamics in voltage and current comparing with the dynamics in the resonant inductor current $i_r(t)$ and resonant capacitor voltage

$v_{\mathrm{Cr}}(t)$. Therefore, only the DC component of the output current diode rectifier $i_{\mathrm{out,Rec}}$ is considered as an output variable which is expressed by i_{o}. Eventually, the output current equation delivered by the SRC# during the K_{th} event is express as

$$\begin{aligned}
i_{\mathrm{o}} &= \frac{1}{\gamma_k}\int_0^{\beta_k} i_{\mathrm{out,Rec}}(\theta_{\mathrm{s}})d\theta_{\mathrm{s}} + \frac{1}{\gamma_k}\int_{\beta_k}^{\gamma_k} i_{\mathrm{out,Rec}}(\theta_{\mathrm{s}})d\theta_{\mathrm{s}} \\
&= \frac{1}{\gamma_k}\cdot\left\{\frac{1}{\omega_{\mathrm{rs}}}\sin(\omega_{\mathrm{rs}}\beta_k) + \frac{1}{\omega_{\mathrm{rs}}}\sin(\omega_{\mathrm{rs}}\beta_K)\cdot\left[1-\cos(\omega_{\mathrm{rs}}\alpha_k)\right]\right\} \\
&\quad\cdot I_{\mathrm{r},0(k)} + \frac{1}{\gamma_k}\cdot\left\{-\frac{1}{\omega_{\mathrm{rs}}}\frac{1}{Z_{\mathrm{r}}}\left[1-\cos(\omega_{\mathrm{rs}}\beta_k)\right] + \frac{1}{\omega_{\mathrm{rs}}}\frac{1}{Z_{\mathrm{r}}}\cos\right. \\
&\quad\left.\cdot(\omega_{\mathrm{rs}}\beta_K)\cdot\left[1-\cos(\omega_{\mathrm{rs}}\alpha_k)\right]\right\}\cdot V_{\mathrm{Cr},0(k)} + \frac{1}{\gamma_k} \\
&\quad\cdot\left\{-\frac{1}{\omega_{\mathrm{rs}}}\frac{1}{Z_{\mathrm{r}}}\left[1-\cos(\omega_{\mathrm{rs}}\beta_k)\right] + \frac{1}{\omega_{\mathrm{rs}}}\frac{1}{Z_{\mathrm{r}}}\left(\cos(\omega_{\mathrm{rs}}\beta_K)-2\right)\right. \\
&\quad\left.\cdot\left[1-\cos(\omega_{\mathrm{rs}}\alpha_k)\right]\right\}\cdot V_{\mathrm{o},0(k)} + \frac{1}{\gamma_k} \\
&\quad\cdot\left\{\frac{1}{\omega_{\mathrm{rs}}}\frac{1}{Z_{\mathrm{r}}}\left[1-\cos(\omega_{\mathrm{rs}}\beta_k)\right] + \frac{1}{\omega_{\mathrm{rs}}}\frac{1}{Z_{\mathrm{r}}}\left(1-\cos(\omega_{\mathrm{rs}}\beta_K)\right)\right. \\
&\quad\left.\cdot\left[1-\cos(\omega_{\mathrm{rs}}\alpha_k)\right]\right\}\cdot V_{\mathrm{g},0(k)},
\end{aligned} \tag{A.17}$$

where

$$\begin{aligned}
\theta_{\mathrm{s}} &= \omega_{\mathrm{s}}t, \\
\alpha_k &= \gamma_k - \beta_k.
\end{aligned} \tag{A.18}$$

It should be noted that the initial value of inductor current is represented by $I_{\mathrm{r},0(k)}$, $V_{\mathrm{Cr},0(k)}$ is the initial value of capacitor voltage, the initial value of rectifier output voltage is written as $V_{\mathrm{o},0(k)}$, and $V_{\mathrm{g},0(k)}$ is then the initial value of input voltage of SRC#. Characteristic impedance Z_{r} is defined by the parameter of resonant tanks ($=\sqrt{L_{\mathrm{r}}C_{\mathrm{r}}}$), α_k is the transistor and diode conduction angle during the switching interval event k, and the switching frequency of the converter is represented by θ_{s} ($=\omega_{\mathrm{s}}\cdot t$). Finally, the steady-state solution of the discrete-state equation for the output variable i_{o} can be obtained by substituting the steady-state condition into (A.17) as

$$\overline{I}_{\mathrm{o}} = i_{\mathrm{o}}\Big|_{\left(\beta_k=\overline{\beta},\alpha_k=\overline{\alpha},\gamma_k=\overline{\gamma},I_{\mathrm{r},0(k)}=\overline{I}_{\mathrm{r}},V_{\mathrm{Cr},0(k)}=\overline{V}_{\mathrm{cr}},V_{\mathrm{o},0(k)}=\overline{V}_{\mathrm{o}},V_{\mathrm{g},0(k)}=\overline{V}_{\mathrm{g}}\right)}. \tag{A.19}$$

Step 5. Define state variable.

Control design technique based on the linear control theory cannot directly be applied for, mainly because of the high nonlinearity in the discrete large-signal state equations in (A.12), (A.13), and (A.17). Therefore, the linearization of the above large-signal equations is necessary. Equation (A.20) shows the definitions of interesting state variables in both k_{th} switching event ($t_{0(k)} \le t \le t_{2(k)}$) and $(k+1)_{\mathrm{th}}$ switching event ($t_{2(k)} \le t \le t_{2(k+1)}$) which is used in the linearization process. Eventually, the following equations of approximation of derivative are applied for converting the discrete large-signal model into the continuous time:

$$\begin{aligned}
x_{1(k)} &= I_{\mathrm{r},0(k)}, \\
x_{2(k)} &= V_{\mathrm{Cr},0(k)}, \\
I_{\mathrm{r},2(k)} &= -x_{1(k+1)}, \\
V_{\mathrm{Cr},2(k)} &= -x_{2(k+1)},
\end{aligned} \tag{A.20}$$

$$\dot{x}_i(t_k) = \frac{x_{i,(k+1)} - x_{i,(k)}}{t_{0(k+1)} - t_{0(k)}} = \frac{\omega_{\mathrm{s}}}{\gamma_k}\left(x_{i,(k+1)} - x_{i,(k)}\right), \tag{A.21}$$

where

$$\gamma_k = \omega_{\mathrm{s}}\left(t_{2(k)} - t_{0(k)}\right) = \omega_{\mathrm{s}}\left(t_{0(k+1)} - t_{0(k)}\right). \tag{A.22}$$

Instead of using the state variables in (A.12) and (A.13), the state variables in (A.12) and (A.13) are replaced by the defined state given in (A.20). With the approximation of derivation in (A.21), the nonlinear state-space model is given by

$$\begin{aligned}
\dot{x}_{1(k)} &= \frac{\omega_{\mathrm{s}}}{\gamma_k}\cdot\left[\sin(\omega_{\mathrm{rs}}\beta_K)\cdot\sin(\omega_{\mathrm{rs}}\alpha_K) - 1\right]\cdot x_{1(k)} \\
&\quad + \frac{\omega_{\mathrm{s}}}{\gamma_k}\cdot\left[\frac{1}{Z_{\mathrm{r}}}\cdot\cos(\omega_{\mathrm{rs}}\beta_K)\cdot\sin(\omega_{\mathrm{rs}}\alpha_K)\right]\cdot x_{2(k)} + \frac{\omega_{\mathrm{s}}}{\gamma_k} \\
&\quad\cdot\left[\frac{-2}{Z_{\mathrm{r}}}\cdot\sin(\omega_{\mathrm{rs}}\alpha_K) + \frac{1}{Z_{\mathrm{r}}}\cdot\cos(\omega_{\mathrm{rs}}\beta_K)\cdot\sin(\omega_{\mathrm{rs}}\alpha_K)\right] \\
&\quad\cdot V_{\mathrm{o},0(k)} + \frac{\omega_{\mathrm{s}}}{\gamma_k}\cdot\left[\frac{1}{Z_{\mathrm{r}}}\cdot\sin(\omega_{\mathrm{rs}}\alpha_K) + \frac{-1}{Z_{\mathrm{r}}}\cdot\cos(\omega_{\mathrm{rs}}\beta_K)\right. \\
&\quad\left.\cdot\sin(\omega_{\mathrm{rs}}\alpha_K)\right]\cdot V_{\mathrm{g},0(k)}, \\
&= f_1\left\{x_{1(k)}, x_{2(k)}, V_{\mathrm{o},0(k)}, V_{\mathrm{g},0(k)}, \alpha_k\right\} \\
&= f_1\left\{x_1, x_2, v_{\mathrm{o}}, v_{\mathrm{g}}, \alpha\right\} \\
&= \frac{\omega_{\mathrm{s}}}{\gamma_k}\cdot f_1^*\left\{x_1, x_2, v_{\mathrm{o}}, v_{\mathrm{g}}, \alpha\right\}, \\
\dot{x}_{2(k)} &= \frac{\omega_{\mathrm{s}}}{\gamma_k}\cdot\left[-Z_{\mathrm{r}}\cdot\sin(\omega_{\mathrm{rs}}\beta_K)\cdot\cos(\omega_{\mathrm{rs}}\alpha_K)\right]\cdot x_{1(k)} \\
&\quad + \frac{\omega_{\mathrm{s}}}{\gamma_k}\cdot\left[-\cos(\omega_{\mathrm{rs}}\beta_K)\cdot\cos(\omega_{\mathrm{rs}}\alpha_K) - 1\right]\cdot x_{2(k)} + \frac{\omega_{\mathrm{s}}}{\gamma_k} \\
&\quad\cdot\left[2\cdot\cos(\omega_{\mathrm{rs}}\alpha_K) - \cos(\omega_{\mathrm{rs}}\beta_K)\cdot\cos(\omega_{\mathrm{rs}}\alpha_K) - 1\right] \\
&\quad\cdot V_{\mathrm{o},0(k)} + \frac{\omega_{\mathrm{s}}}{\gamma_k}\cdot\left[-\cos(\omega_{\mathrm{rs}}\alpha_K) + \cos(\omega_{\mathrm{rs}}\beta_K)\right. \\
&\quad\left.\cdot\cos(\omega_{\mathrm{rs}}\alpha_K)\right]\cdot V_{\mathrm{g},0(k)}, \\
&= f_2\left\{x_{1(k)}, x_{2(k)}, V_{\mathrm{o},0(k)}, V_{\mathrm{g},0(k)}, \alpha_k\right\} \\
&= f_2\left\{x_1, x_2, v_{\mathrm{o}}, v_{\mathrm{g}}, \alpha\right\} \\
&= \frac{\omega_{\mathrm{s}}}{\gamma_k}\cdot f_2^*\left\{x_1, x_2, v_{\mathrm{o}}, v_{\mathrm{g}}, \alpha\right\},
\end{aligned} \tag{A.23}$$

where the output equation is

$$\begin{aligned} i_o &= f_{out}\{x_{1(k)}, x_{2(k)}, V_{o,0(k)}, V_{g,0(k)}, \alpha_k\}, \\ &= f_{out}\{x_1, x_2, v_o, v_g, \alpha\} \\ &= \frac{1}{\gamma_k}\cdot f^*_{out}\{x_1, x_2, v_o, v_g, \alpha\}. \end{aligned} \tag{A.24}$$

Step 6. Linearization and small-signal model.

Inject a small perturbation in all the interesting state variables in Step 5 during the steady state (near the certain operating point, OP). The nonlinear state equations can be rewritten with *Taylor series expansion* in terms of the operating point (OP) and the perturbations:

(i) Taylor series expansion of resonant inductor current:

$$\begin{aligned} [\dot{\overline{x}}_1 + \dot{\tilde{x}}_1] &= f_1\{\overline{x}_1 + \tilde{x}_1, \overline{x}_2 + \tilde{x}_2, \overline{V}_o + \tilde{V}_o, \overline{V}_g \\ &\quad + \tilde{V}_g, \overline{\alpha} + \tilde{\alpha}\}, \\ &= \frac{\omega_s}{\gamma_k}\cdot f^*_1\{\overline{x}_1 + \tilde{x}_1, \overline{x}_2 + \tilde{x}_2, \overline{V}_o + \tilde{V}_o, \overline{V}_g \\ &\quad + \tilde{V}_g, \overline{\alpha} + \tilde{\alpha}\}, \end{aligned} \tag{A.25}$$

where

$$\begin{aligned} x_1 &= \overline{x}_1 + \tilde{x}_1, \\ x_2 &= \overline{x}_2 + \tilde{x}_2, \\ v_g &= \overline{V}_g + \tilde{V}_g, \\ v_o &= \overline{V}_o + \tilde{V}_o, \\ \alpha &= \overline{\alpha} + \tilde{\alpha}, \end{aligned} \tag{A.26}$$

then

$$\begin{aligned} [\dot{\overline{x}}_1 + \dot{\tilde{x}}_1] &= f_1\{\overline{x}_1, \overline{x}_2, \overline{V}_o, \overline{V}_g, \overline{\alpha}\} + \left.\frac{\partial f_1}{\partial x_1}\right|_{OP}\tilde{x}_1 \\ &\quad + \left.\frac{\partial f_1}{\partial x_2}\right|_{OP}\tilde{x}_2 + \left.\frac{\partial f_1}{\partial v_g}\right|_{OP}\tilde{V}_g + \left.\frac{\partial f_1}{\partial v_o}\right|_{OP}\tilde{V}_o \\ &\quad + \left.\frac{\partial f_1}{\partial \alpha}\right|_{OP}\tilde{\alpha} + \frac{1}{2!}\left.\frac{\partial^2 f}{\partial x_1^2}\right|_{OP}\tilde{x}_1^2 + \cdots, \end{aligned} \tag{A.27}$$

where the subscript OP in equations indicate that the equation is evaluated at that steady-state point:

$$\begin{aligned} &OP = \overline{I}_r, \overline{V}_{Cr}, \overline{V}_o, \overline{V}_g, \overline{\alpha}, \\ &f_1\{\overline{x}_1, \overline{x}_2, \overline{V}_o, \overline{V}_g, \overline{\alpha}\} = \dot{\overline{I}}_r = 0. \end{aligned} \tag{A.28}$$

(ii) Taylor series expansion of resonant capacitor voltage:

$$\begin{aligned} [\dot{\overline{x}}_2 + \dot{\tilde{x}}_2] &= f_2\{\overline{x}_1 + \tilde{x}_1, \overline{x}_2 + \tilde{x}_2, \overline{V}_o + \tilde{V}_o, \overline{V}_g \\ &\quad + \tilde{V}_g, \overline{\alpha} + \tilde{\alpha}\}, \\ &= \frac{\omega_s}{\gamma_k}\cdot f^*_2\{\overline{x}_1 + \tilde{x}_1, \overline{x}_2 + \tilde{x}_2, \overline{V}_o + \tilde{V}_o, \overline{V}_g \\ &\quad + \tilde{V}_g, \overline{\alpha} + \tilde{\alpha}\}, \end{aligned} \tag{A.29}$$

where

$$\begin{aligned} x_1 &= \overline{x}_1 + \tilde{x}_1, \\ x_2 &= \overline{x}_2 + \tilde{x}_2, \\ v_g &= \overline{V}_g + \tilde{V}_g, \\ v_o &= \overline{V}_o + \tilde{V}_s, \\ \alpha &= \overline{\alpha} + \tilde{\alpha}, \end{aligned} \tag{A.30}$$

then

$$\begin{aligned} [\dot{\overline{x}}_2 + \dot{\tilde{x}}_2] &= f_2\{\overline{x}_1, \overline{x}_2, \overline{V}_o, \overline{V}_g, \overline{\alpha}\} + \left.\frac{\partial f_2}{\partial x_1}\right|_{OP}\tilde{x}_1 \\ &\quad + \left.\frac{\partial f_2}{\partial x_2}\right|_{OP}\tilde{x}_2 + \left.\frac{\partial f_2}{\partial v_g}\right|_{OP}\tilde{V}_g + \left.\frac{\partial f_2}{\partial v_o}\right|_{OP}\tilde{V}_o \\ &\quad + \left.\frac{\partial f_2}{\partial \alpha}\right|_{OP}\tilde{\alpha} + \frac{1}{2!}\left.\frac{\partial^2 f_2}{\partial x_1^2}\right|_{OP}\tilde{x}_1^2 + \cdots, \end{aligned} \tag{A.31}$$

where

$$f_2\{\overline{x}_1, \overline{x}_2, \overline{V}_o, \overline{V}_g, \overline{\alpha}\} = \dot{\overline{V}}_{Cr} = 0. \tag{A.32}$$

(iii) Taylor series expansion of the output current equation:

$$\begin{aligned} \overline{I}_o + \tilde{I}_o &= f_{out}\{\overline{x}_1 + \tilde{x}_1, \overline{x}_2 + \tilde{x}_2, \overline{V}_o + \tilde{V}_o, \overline{V}_g + \tilde{V}_g, \overline{\alpha} + \tilde{\alpha}\}, \\ &= \frac{1}{(\overline{\gamma} + \tilde{\gamma})}\cdot f^*_{out}\{\overline{x}_1 + \tilde{x}_1, \overline{x}_2 + \tilde{x}_2, \overline{V}_o + \tilde{V}_o, \overline{V}_g \\ &\quad + \tilde{V}_g, \overline{\alpha} + \tilde{\alpha}\}, \end{aligned} \tag{A.33}$$

where

$$\begin{aligned} x_1 &= \overline{x}_1 + \tilde{x}_1, \\ x_2 &= \overline{x}_2 + \tilde{x}_2, \\ v_g &= \overline{V}_g + \tilde{V}_g, \\ v_o &= \overline{V}_o + \tilde{V}_o, \\ \alpha &= \overline{\alpha} + \tilde{\alpha}, \\ \tilde{\gamma} &= \tilde{\alpha} + \tilde{\beta}, \end{aligned} \tag{A.34}$$

then

$$\begin{aligned}\overline{I}_{\mathrm{o}}+\widetilde{I}_{\mathrm{o}} &= f_{\mathrm{out}}\left\{\overline{x}_1,\overline{x}_2,\overline{V}_{\mathrm{o}},\overline{V}_{\mathrm{g}},\overline{\alpha}\right\}+\left.\frac{\partial f_{\mathrm{out}}}{\partial x_1}\right|_{\mathrm{OP}}\widetilde{x}_1\\ &\quad+\left.\frac{\partial f_{\mathrm{out}}}{\partial x_2}\right|_{\mathrm{OP}}\widetilde{x}_2+\left.\frac{\partial f_{\mathrm{out}}}{\partial v_{\mathrm{g}}}\right|_{\mathrm{OP}}\widetilde{V}_{\mathrm{g}}+\left.\frac{\partial f_{\mathrm{out}}}{\partial v_{\mathrm{o}}}\right|_{\mathrm{OP}}\widetilde{V}_{\mathrm{o}}\\ &\quad+\left.\frac{\partial f_{\mathrm{out}}}{\partial \alpha}\right|_{\mathrm{OP}}\widetilde{\alpha}+\frac{1}{2!}\left.\frac{\partial^2 f_{\mathrm{out}}}{\partial x_1^2}\right|_{\mathrm{OP}}\widetilde{x}_1^2+\cdots,\\ &=\frac{1}{\overline{\gamma}}\cdot\left\{1-\left(\frac{\widetilde{\gamma}}{\overline{\gamma}}\right)+\left(\frac{\widetilde{\gamma}}{\overline{\gamma}}\right)^2-\cdots+\cdots\right\}\\ &\quad\cdot\left\{f_{\mathrm{out}}^*\left\{\overline{x}_1,\overline{x}_2,\overline{V}_{\mathrm{o}},\overline{V}_{\mathrm{g}},\overline{\alpha}\right\}+\left.\frac{\partial f_{\mathrm{out}}^*}{\partial x_1}\right|_{\mathrm{OP}}\widetilde{x}_1\left.\frac{\partial f_{\mathrm{out}}^*}{\partial x_2}\right|_{\mathrm{OP}}\right.\\ &\quad\cdot\widetilde{x}_2+\left.\frac{\partial f_{\mathrm{out}}^*}{\partial v_{\mathrm{g}}}\right|_{\mathrm{OP}}\widetilde{V}_{\mathrm{g}}+\left.\frac{\partial f_{\mathrm{out}}}{\partial v_{\mathrm{o}}}\right|_{\mathrm{OP}}\widetilde{V}_{\mathrm{o}}+\left.\frac{\partial f_{\mathrm{out}}^*}{\partial \alpha}\right|_{\mathrm{OP}}\widetilde{\alpha}\\ &\quad+\frac{1}{2!}\left.\frac{\partial^2 f_{\mathrm{out}}^*}{\partial x_1^2}\right|_{\mathrm{OP}}\widetilde{x}_1^2+\cdots\Bigg\},\end{aligned}\tag{A.35}$$

where

$$\begin{aligned}\overline{I}_{\mathrm{o}} &= f_{\mathrm{out}}\left\{\overline{x}_1,\overline{x}_2,\overline{V}_{\mathrm{o}},\overline{V}_{\mathrm{g}},\overline{\alpha}\right\},\\ \widetilde{I}_{\mathrm{o}} &= \frac{1}{\overline{\gamma}}\cdot\left\{\left[\left.\frac{\partial f_{\mathrm{out}}^*}{\partial x_1}\right|_{\mathrm{OP}}-\overline{I}_{\mathrm{o}}\cdot\left.\frac{\partial\beta}{\partial x_1}\right|_{\mathrm{OP}}\right]\cdot\widetilde{x}_1\right.\\ &\quad+\left[\left.\frac{\partial f_{\mathrm{out}}^*}{\partial x_2}\right|_{\mathrm{OP}}-\overline{I}_{\mathrm{o}}\cdot\left.\frac{\partial\beta}{\partial x_2}\right|_{\mathrm{OP}}\right]\cdot\widetilde{x}_2\\ &\quad+\left[\left.\frac{\partial f_{\mathrm{out}}^*}{\partial v_{\mathrm{g}}}\right|_{\mathrm{OP}}-\overline{I}_{\mathrm{o}}\cdot\left.\frac{\partial\beta}{\partial v_{\mathrm{g}}}\right|_{\mathrm{OP}}\right]\cdot\widetilde{V}_{\mathrm{g}}\\ &\quad+\left[\left.\frac{\partial f_{\mathrm{out}}^*}{\partial v_{\mathrm{o}}}\right|_{\mathrm{OP}}-\overline{I}_{\mathrm{o}}\cdot\left.\frac{\partial\beta}{\partial v_{\mathrm{o}}}\right|_{\mathrm{OP}}\right]\cdot\widetilde{V}_{\mathrm{o}}\\ &\quad+\left[\left.\frac{\partial f_{\mathrm{out}}^*}{\partial \alpha}\right|_{\mathrm{OP}}-\overline{I}_{\mathrm{o}}\right]\cdot\widetilde{\alpha}\Bigg\}.\end{aligned}\tag{A.36}$$

The linearized equations can be obtained by neglecting the higher order terms of perturbation signals and retaining only the linear terms in the *Taylor series expansion* for (A.27), (A.31), and (A.35).

Step 7. State-space model.

A set of the linearized state-space model (in (A.37)) of SRC# in the subresonant mode can be generated from (A.27), (A.31), and (A.35). Additionally, the expression of transfer functions between the input state variables and the interesting state variables are given in (A.44) and (A.46):

$$\begin{aligned}\begin{bmatrix}\dot{\widetilde{x}}_1\\ \dot{\widetilde{x}}_2\end{bmatrix} &= \begin{bmatrix}\left.\frac{\partial f_1}{\partial x_1}\right|_{\mathrm{OP}} & \left.\frac{\partial f_1}{\partial x_2}\right|_{\mathrm{OP}}\\ \left.\frac{\partial f_2}{\partial x_1}\right|_{\mathrm{OP}} & \left.\frac{\partial f_2}{\partial x_2}\right|_{\mathrm{OP}}\end{bmatrix}\begin{bmatrix}\widetilde{x}_1\\ \widetilde{x}_2\end{bmatrix}+\begin{bmatrix}\left.\frac{\partial f_1}{\partial \alpha}\right|_{\mathrm{OP}} & \left.\frac{\partial f_1}{\partial v_{\mathrm{g}}}\right|_{\mathrm{OP}} & \left.\frac{\partial f_1}{\partial v_{\mathrm{o}}}\right|_{\mathrm{OP}}\\ \left.\frac{\partial f_2}{\partial \alpha}\right|_{\mathrm{OP}} & \left.\frac{\partial f_2}{\partial v_{\mathrm{g}}}\right|_{\mathrm{OP}} & \left.\frac{\partial f_2}{\partial v_{\mathrm{o}}}\right|_{\mathrm{OP}}\end{bmatrix}\begin{bmatrix}\widetilde{\alpha}\\ \widetilde{V}_{\mathrm{g}}\\ \widetilde{V}_{\mathrm{o}}\end{bmatrix},\\ \widetilde{I}_{\mathrm{o}} &= \left[\frac{1}{\overline{\gamma}}\cdot\left[\left.\frac{\partial f_{\mathrm{out}}^*}{\partial x_1}\right|_{\mathrm{OP}}-\overline{I}_{\mathrm{o}}\cdot\left.\frac{\partial\beta}{\partial x_1}\right|_{\mathrm{OP}}\right]\ \frac{1}{\overline{\gamma}}\cdot\left[\left.\frac{\partial f_{\mathrm{out}}^*}{\partial x_2}\right|_{\mathrm{OP}}-\overline{I}_{\mathrm{o}}\cdot\left.\frac{\partial\beta}{\partial x_2}\right|_{\mathrm{OP}}\right]\right]\\ &\quad\cdot\begin{bmatrix}\widetilde{x}_1\\ \widetilde{x}_2\end{bmatrix}+\left[\frac{1}{\overline{\gamma}}\cdot\left[\left.\frac{\partial f_{\mathrm{out}}^*}{\partial \alpha}\right|_{\mathrm{OP}}-\overline{I}_{\mathrm{o}}\right]\frac{1}{\overline{\gamma}}\right.\\ &\quad\cdot\left[\left.\frac{\partial f_{\mathrm{out}}^*}{\partial v_{\mathrm{g}}}\right|_{\mathrm{OP}}-\overline{I}_{\mathrm{o}}\cdot\left.\frac{\partial\beta}{\partial v_{\mathrm{g}}}\right|_{\mathrm{OP}}\right]\frac{1}{\overline{\gamma}}\cdot\left[\left.\frac{\partial f_{\mathrm{out}}}{\partial v_{\mathrm{o}}}\right|_{\mathrm{OP}}-\overline{I}_{\mathrm{o}}\cdot\left.\frac{\partial\beta}{\partial v_{\mathrm{o}}}\right|_{\mathrm{OP}}\right]\Bigg]\\ &\quad\cdot\begin{bmatrix}\widetilde{\alpha}\\ \widetilde{V}_{\mathrm{g}}\\ \widetilde{V}_{\mathrm{o}}\end{bmatrix}.\end{aligned}\tag{A.37}$$

For derivative of equations f_1 and f_2,

$$\left.\frac{\partial f_i}{\partial x_j}\right.=\left(\frac{\partial}{\partial x_j}\frac{\omega_{\mathrm{s}}}{\gamma}\right)\cdot f_i^*\Big|_{\mathrm{OP}}+\left.\frac{\omega_{\mathrm{s}}}{\gamma}\frac{\partial f_i^*}{\partial x_j}\right|_{\mathrm{OP}},\tag{A.38}$$

where

$$\gamma=\alpha+\beta\quad\text{for } i=1,2,\ \ j=1,2.\tag{A.39}$$

With the steady-state operating conditions,

$$\begin{aligned}\left.\frac{\omega_{\mathrm{s}}}{\gamma}\right|_{\mathrm{OP}}&\neq 0,\\ f_i^*\big|_{\mathrm{OP}}&=0.\end{aligned}\tag{A.40}$$

Therefore,

$$\left.\frac{\partial f_i}{\partial x_j}\right.=\left.\frac{\omega_{\mathrm{s}}}{\gamma}\frac{\partial f_i^*}{\partial x_j}\right|_{\mathrm{OP}}.\tag{A.41}$$

The same derivation process, which are used to the derivatives of f_1 and f_2 with respect to input states x_1 and x_2 can be used to calculate the derivative of f_{out}^* in the output equation and the derivatives of f_1 and f_2 with respect to input states α, v_{g}, and v_{o}. Additionally, the angle β and its steady-state solution can be calculated by the derivation of the large-signal model in (A.7) as

$$\begin{aligned}\tan\left(\omega_{\mathrm{rs}}\beta\right)&=\frac{-x_1Z_{\mathrm{r}}}{\left(v_{\mathrm{g}}-v_{\mathrm{o}}-x_2\right)}=\tan\left(\omega_{\mathrm{rs}}\beta-\pi\right),\\ \beta|_{\mathrm{OP}}&=\frac{\pi}{\omega_{\mathrm{rs}}}+\frac{1}{\omega_{\mathrm{rs}}}\cdot\tan^{-1}\left[\frac{-\overline{I}_{\mathrm{r}}Z_{\mathrm{r}}}{\left(\overline{V}_{\mathrm{g}}-\overline{V}_{\mathrm{o}}-\overline{V}_{\mathrm{Cr}}\right)}\right].\end{aligned}\tag{A.42}$$

The derivative of β with respect to input states x_1, x_2, v_{g}, and v_{o} at the given operating points is expressed by the following equation:

$$\left.\frac{\partial\beta}{\partial x_1}\right|_{\mathrm{OP}}=\left[\frac{1}{\omega_{\mathrm{rs}}}\cdot\frac{-Z_{\mathrm{r}}\cdot\left(v_{\mathrm{g}}-v_{\mathrm{o}}-x_2\right)}{\left(v_{\mathrm{g}}-v_{\mathrm{o}}-x_2\right)^2+\left(x_1Z_{\mathrm{r}}\right)^2}\right]\Bigg|_{\mathrm{OP}}$$
$$=\frac{1}{\omega_{\mathrm{rs}}}\cdot\frac{-Z_{\mathrm{r}}\cdot\left(\overline{V}_{\mathrm{g}}-\overline{V}_{\mathrm{o}}-\overline{V}_{\mathrm{Cr}}\right)}{\left(\overline{V}_{\mathrm{g}}-\overline{V}_{\mathrm{o}}-\overline{V}_{\mathrm{Cr}}\right)^2+\left(\overline{I}_{\mathrm{r}}Z_{\mathrm{r}}\right)^2},$$
$$\left.\frac{\partial\beta}{\partial x_2}\right|_{\mathrm{OP}}=\left[\frac{1}{\omega_{\mathrm{rs}}}\cdot\frac{-x_1Z_{\mathrm{r}}}{\left(v_{\mathrm{g}}-v_{\mathrm{o}}-x_2\right)^2+\left(x_1Z_{\mathrm{r}}\right)^2}\right]\Bigg|_{\mathrm{OP}}$$
$$=\frac{1}{\omega_{\mathrm{rs}}}\cdot\frac{-\overline{I}_{\mathrm{r}}Z_{\mathrm{r}}}{\left(\overline{V}_{\mathrm{g}}-\overline{V}_{\mathrm{o}}-\overline{V}_{\mathrm{Cr}}\right)^2+\left(\overline{I}_{\mathrm{r}}Z_{\mathrm{r}}\right)^2},$$
$$\left.\frac{\partial\beta}{\partial v_{\mathrm{o}}}\right|_{\mathrm{OP}}=\left[\frac{1}{\omega_{\mathrm{rs}}}\cdot\frac{-x_1Z_{\mathrm{r}}}{\left(v_{\mathrm{g}}-v_{\mathrm{o}}-x_2\right)^2+\left(x_1Z_{\mathrm{r}}\right)^2}\right]\Bigg|_{\mathrm{OP}}$$
$$=\frac{1}{\omega_{\mathrm{rs}}}\cdot\frac{-\overline{I}_{\mathrm{r}}Z_{\mathrm{r}}}{\left(\overline{V}_{\mathrm{g}}-\overline{V}_{\mathrm{o}}-\overline{V}_{\mathrm{Cr}}\right)^2+\left(\overline{I}_{\mathrm{r}}Z_{\mathrm{r}}\right)^2},$$
$$\left.\frac{\partial\beta}{\partial v_{\mathrm{g}}}\right|_{\mathrm{OP}}=\left[\frac{1}{\omega_{\mathrm{rs}}}\cdot\frac{x_1Z_{\mathrm{r}}}{\left(v_{\mathrm{g}}-v_{\mathrm{o}}-x_2\right)^2+\left(x_1Z_{\mathrm{r}}\right)^2}\right]\Bigg|_{\mathrm{OP}}$$
$$=\frac{1}{\omega_{\mathrm{rs}}}\cdot\frac{\overline{I}_{\mathrm{r}}Z_{\mathrm{r}}}{\left(\overline{V}_{\mathrm{g}}-\overline{V}_{\mathrm{o}}-\overline{V}_{\mathrm{Cr}}\right)^2+\left(\overline{I}_{\mathrm{r}}Z_{\mathrm{r}}\right)^2},\tag{A.43}$$

where ω_{rs} ($=\omega_{\mathrm{r}}/\omega_{\mathrm{s}}$) is defined by the ratio between the natural frequency of the resonant tank (ω_{r}) and the switching frequency of SRC# (ω_{s}).

Step 8. Transfer functions.

According to (A.37), the transfer functions between the converter output current (output rectifier current) and input state variables can be obtained:

$$\widetilde{I}_{\mathrm{o}}(s)=\begin{bmatrix}g_1(s) & g_2(s) & g_3(s)\end{bmatrix}\begin{bmatrix}\widetilde{\alpha}\\ \widetilde{V}_{\mathrm{g}}\\ \widetilde{V}_{\mathrm{o}}\end{bmatrix},\tag{A.44}$$

where

$$g_1(s)=\left.\frac{\widetilde{I}_{\mathrm{o}}(s)}{\widetilde{\alpha}(s)}\right|_{\widetilde{V}_{\mathrm{g}}(s)=0,\widetilde{V}_{\mathrm{o}}(s)=0},$$
$$g_2(s)=\left.\frac{\widetilde{I}_{\mathrm{o}}(s)}{\widetilde{V}_{\mathrm{g}}(s)}\right|_{\widetilde{\alpha}(s)=0,\widetilde{V}_{\mathrm{o}}(s)=0},$$
$$g_3(s)=\left.\frac{\widetilde{I}_{\mathrm{o}}(s)}{\widetilde{V}_{\mathrm{o}}(s)}\right|_{\widetilde{\alpha}(s)=0,\widetilde{V}_{\mathrm{g}}(s)=0},\tag{A.45}$$
$$\widetilde{f}_s=\widetilde{\alpha}(s)\cdot\frac{f_{\mathrm{r}}}{-\pi},$$

and transfer functions between defined internal state variables and input state are

$$\widetilde{X}=\begin{bmatrix}\widetilde{I}_{\mathrm{r}}\\ \widetilde{v}_{\mathrm{Cr}}\end{bmatrix}=\begin{bmatrix}\widetilde{x}_1\\ \widetilde{x}_2\end{bmatrix}=\begin{bmatrix}g_{\mathrm{xu},11} & g_{\mathrm{xu},12} & g_{\mathrm{xu},13}\\ g_{\mathrm{xu},21} & g_{\mathrm{xu},22} & g_{\mathrm{xu},23}\end{bmatrix}\begin{bmatrix}\widetilde{\alpha}\\ \widetilde{V}_{\mathrm{g}}\\ \widetilde{V}_{\mathrm{o}}\end{bmatrix},\tag{A.46}$$

where

$$\begin{cases}g_{\mathrm{xu},11}=\left.\dfrac{\widetilde{I}_{\mathrm{r}}}{\widetilde{\alpha}}\right|_{\widetilde{V}_{\mathrm{g}}(s)=0,\widetilde{V}_{\mathrm{o}}(s)=0},\\ g_{\mathrm{xu},12}=\left.\dfrac{\widetilde{I}_{\mathrm{r}}}{\widetilde{V}_{\mathrm{g}}}\right|_{\widetilde{\alpha}(s)=0,\widetilde{V}_{\mathrm{o}}(s)=0},\\ g_{\mathrm{xu},13}=\left.\dfrac{\widetilde{I}_{\mathrm{r}}}{\widetilde{V}_{\mathrm{o}}}\right|_{\widetilde{\alpha}(s)=0,\widetilde{V}_{\mathrm{g}}(s)=0},\\ g_{\mathrm{xu},21}=\left.\dfrac{\widetilde{v}_{\mathrm{Cr}}}{\widetilde{\alpha}}\right|_{\widetilde{V}_{\mathrm{g}}(s)=0,\widetilde{V}_{\mathrm{o}}(s)=0},\\ g_{\mathrm{xu},22}=\left.\dfrac{\widetilde{v}_{\mathrm{Cr}}}{\widetilde{V}_{\mathrm{g}}}\right|_{\widetilde{\alpha}(s)=0,\widetilde{V}_{\mathrm{o}}(s)=0},\\ g_{\mathrm{xu},23}=\left.\dfrac{\widetilde{v}_{\mathrm{Cr}}}{\widetilde{V}_{\mathrm{o}}}\right|_{\widetilde{\alpha}(s)=0,\widetilde{V}_{\mathrm{g}}(s)}.\end{cases}\tag{A.47}$$

The details of derivation of the linearized plant model and the expression of elements in matrixes $[A]$, $[B]$, $[C]$, and $[D]$ are shown in (A.37), where the expressions of transfer functions, $g_1(s)$, $g_2(s)$, and $g_3(s)$, in (A.44) can be obtained by (3).

B. Derivation of Output LC Filter

Step 9. Derivation of transfer function of output LC filter.

The output current of SRC# delivered from the output diode rectifier to the MVDC grid has a high-harmonic content at twice the switching frequency and its multiples, and at the moment, only the mean value of the output current in one event is considered as the real output current. An output LC filter has to be placed on the output terminal of the converter in order to decrease as much as possible the current harmonics and mitigate the inrush current during fault. The following equations give the transfer functions of the output LC filter used to derive the harmonic model of the DC turbine converter:

$$g_{f1} = \frac{\widetilde{I}_{turb}}{\widetilde{I}_{o,Rec}} = \frac{R_C/(R_C + R_L)}{1 + s \cdot ((L_f + R_C R_L C_f)/(R_C + R_L)) + s^2 \cdot ((L_f C_f R_C)/(R_C + R_L))},$$

$$g_{f2} = \frac{\widetilde{V}_{o,Rec}}{\widetilde{I}_{o,Rec}} = \frac{R_C R_C + R_L (1 + s(L_f/R_L))}{1 + s \cdot ((L_f + R_C R_L C_f)/(R_C + R_L)) + s^2 \cdot ((L_f C_f R_C)/(R_C + R_L))},$$

$$g_{f3} = \frac{\widetilde{I}_{turb}}{\widetilde{V}_{turb}} = \frac{(R_C/(R_C + R_L)) \cdot (1 + sR_C C_f)}{1 + s \cdot ((L_f + R_C R_L C_f)/(R_C + R_L)) + s^2 \cdot ((L_f C_f R_C)/(R_C + R_L))},$$

$$g_{f4} = \frac{\widetilde{V}_{o,Rec}}{\widetilde{V}_g} = \frac{R_C/(R_C + R_L)}{1 + s \cdot ((L_f + R_C R_L C_f)/(R_C + R_L)) + s^2 \cdot ((L_f C_f R_C)/(R_C + R_L))}, \quad \text{(B.1)}$$

where R_C and R_L are the parasitic resistances of filters, and filter capacitance and filter inductance are represented by C_f and L_f, respectively. $\widetilde{V}_{turb}$ ($=\widetilde{V}_{MVDC}$) is the MVDC-side voltage, $\widetilde{V}_{o,Rec}$ is the output diode rectifier voltage of SRC#, and $\widetilde{V}_g$ ($=\widetilde{V}_{LVDC}$) is the LVDC-side voltage of SRC#. The dynamic model of the output LC filter in the control block is given by Figure 7.

C. Control Design of SRC#

Steps 10 and 12. Control design of DC wind turbine converter.

Main specifications for the design of the controller are addressed in articles [47, 48]. Since this is the first paper to address the closed-loop control of the DC wind turbine and then conductor to the susceptibility study of offshore DC wind farm, the paper did not provide specific numbers (/range) for control design of the DC wind turbine in the offshore wind farm. The following descriptions mainly focus on the identification of the coefficient of transfer function $g_c(s)$ of the SRC# turbine converter, and thus it can give the readers a full freedom of control design related to the DC turbine in the offshore wind farms to meet the performance requirements such as stability, zero steady-state error, settling time, overshoot and ringing, and disturbances rejection capability.

According to the structure of the control block in Figure 7, the control deign of SRC# $g_c(s)$ is influenced by the plant model and output LC filter $H(s)$ where the open-loop transfer function $T(s)$ is defined as

$$T(s) = g_C \cdot H(s), \quad \text{(C.1)}$$

where the current delivered to the MVDC grid is related with the switching frequency of the converter by the transfer function $H(s)$ is represented by

$$H(s) = \frac{\widetilde{i}_{turb}}{\widetilde{f}_s} = \frac{g_1 \cdot g_{f1}}{1 - g_{f2} \cdot g_3}. \quad \text{(C.2)}$$

The design of control loop $g_c(s)$ starts by evaluating the frequency response of $H(s)$. At the resonant frequency (≈100 Hz) of the output LC filter, a peak on the magnitude occurs. The parasitic resistances of the capacitor C_f and inductor L_f can provide a limited damper to attenuate the resonant peak.

Following the specifications mentioned at the beginning of this subsection, the design of the controller starts by adding an integrator to minimize steady-state error with a step input. Thus, the output current will reach the reference value with a minimized tracking error after the transient.

Second, a pole around the resonant frequency of the output LC filter is added to lower the resonant magnitude peak influence of the filter.

Third, a gain K is necessary to set a proper crossover frequency f_c which is always lower than the resonant frequency of the output LC filter; otherwise, the resonant peak will be present in the feedback loop and the phase margin of the open-loop transfer function $H(s)$ will be less than 0°, leading to the instability of the closed-loop system. Finally, the generic expression of the transfer function of the designed controller g_C can be expressed as

$$g_C = \frac{K}{s \cdot \left(1 - \left(s/\omega_p\right)\right)}, \quad \text{(C.3)}$$

where K is the gain (Hz/A) of the controller and ω_p is a pole (rad/s) close to the resonant frequency of the output LC filter. In order to improve the transient response of the system and to reject harmonic disturbances, generally, the angular crossover frequency ω_c ($=2\pi \cdot f_c$) of $H(s)$ should be as high as possible. Typically, the selected crossover frequencies f_c for all the operating points, are always less than 10% of the switching frequency f_s ($f_c < 0.1\ f_s$) in order to minimize the influence from the switching harmonics [48]. The crossover frequency of the open-loop transfer function $H(s)$, which can be assumed equal to the bandwidth of the system, characterizes the rapidity of the feedback system. Therefore, the higher the crossover frequency, the faster the response of the system is.

Nomenclature

L_r: Inductor in the resonant tank
C_r: Capacitor in the resonant tank
i_r: Resonant inductor current
v_{Cr}: Resonant capacitor voltage
v_g: Input voltage of the resonant tank referred to the secondary side of the medium-frequency transformer
v_o: Output voltage of the resonant tank

V_{LVDC}: Low-voltage DC
V_{MVDC}: Medium-voltage DC
v_{turb}: Output terminal voltage of the DC wind turbine converter
i_{turb}: Output current of the DC wind turbine converter ($= i_{Lf}$)
$i_{o,Rec}$: Output current of the diode rectifier of the DC wind turbine converter
$v_{o,Rec}$: Output voltage of the diode rectifier of the DC wind turbine converter ($= v_{Cf}$)
L_f: Inductor in the output filter
C_f: Capacitor in the output filter
f_s: Switching frequency of the series resonant converter defined by $= \omega_s/2\pi$
ω_r: Natural resonant frequency of the tank defined by $\omega_r = 1/\sqrt{L_r C_r}$.

Data Availability

The data used to support the findings of this study are available from the corresponding author upon request.

Conflicts of Interest

The authors declare that they have no conflicts of interest.

References

[1] Y.-H. Chen, C. G. Dincan, R. J. Olsen, M. C. Schimmelmann, P. C. Kjær, and C. L. Bak, "Studies for characterisation of electrical properties of DC collection system in offshore wind farms," in *Proceedings of CIGRÉ General Session 2016, B4-301*, Paris, France, August 2016.

[2] T. Christ, S. Seman, and R. Zurowski, "Investigation of DC converter nonlinear interaction with offshore wind power park system," in *Proceedings of EWEA Off-Shore 2015*, pp. 1/4–4/4, Copenhagen, Denmark, March 2015.

[3] C. Meyer and R. W. De Doncker, "Design of a three-phase series resonant converter for offshore DC grids," in *Proceedings of 42nd IAS Annual Meeting; Industry Applications Conference*, pp. 216–223, September 2007.

[4] C. Meyer, *Key components for future offshore dc grids*, Ph.D. dissertation, Institute for Power Electronics and Electrical Drives, RWTH Aachen University, Aachen, Germany, 2007.

[5] S. Vogel, "*Investigation of DC collection network for offshore wind farms*," M.S. thesis, Department of Wind Energy, Technical University of Denmark, Kongens Lyngby, Denmark, 2014.

[6] V. Vorperian and S. Cuk, "A complete DC analysis of the series resonant converter," in *Proceedings of 13th Annual Power Electronics Specialists Conference (PESC'82)*, pp. 85–100, Cambridge, MA, USA, June 1982.

[7] A. F. Wittulski and R. W. Erickson, "Steady-state analysis of the series resonant converter," *IEEE Transactions on Aerospace and Electronic Systems*, vol. AES-21, no. 6, pp. 791–799, 1985.

[8] R. U. Lenke, J. Hu, and R. W. De Doncker, "Unified steady-state description of phase-shift-controlled ZVS-operated series-resonant and non-resonant single-active-bridge converters," in *Proceedings of IEEE Energy Conversion Congress and Exposition (IEEE-ECCE)*, pp. 796–803, IEEE, San Jose, CA, USA, September 2009.

[9] G. Ortiz, H. Uemura, D. Bortis, J. W. Kolar, and O. Apeldoorn, "Modeling of soft-switching losses of IGBTs in high-power high-efficiency dual-active-bridge DC/DC converters," *IEEE Transactions on Electron Devices*, vol. 60, no. 2, pp. 587–597, 2013.

[10] C. G. Dincan, P. Kjær, Y. Chen et al., "Design of a high power, resonant converter for DC wind turbines," *IEEE Transactions on Power Electronics*, 2018.

[11] P. C. Kjær, C. L. Bak, P. F. M. Da Silva, Y. H. Chen, and C. G. Dincan, "Power collection and distribution in medium voltage DC networks," 2015, http://www.dcc.et.aau.dk.

[12] C. Dincan, P. C. Kjær, Y. H. Chen, S. Munk-Nielsen, and C. L. Bak, "High power, medium voltage, series resonant converter for DC wind turbines," *IEEE Transactions on Power Electronics*, vol. 33, no. 9, pp. 7455–7465, 2018.

[13] D. Jovcic, "Step-up DC-DC converter for megawatt size applications," *IET Power Electronics*, vol. 2, no. 6, pp. 675–685, 2009.

[14] D. Jovcic, "Bidirectional, high-power DC-transformer," *IEEE Transactions on Power Delivery*, vol. 25, no. 4, pp. 2276–2283, 2010.

[15] W. Chen, A. Q. Huan, C. Li, G. Wang, and W. Gu, "Analysis and comparison of medium voltage high power DC/DC converters for offshore wind energy systems," *IEEE Transactions on Power Electronics*, vol. 28, no. 4, pp. 2014–2023, 2013.

[16] A. Parastar and J. K. Seok, "High gain resonant switched capacitor cell based DC/DC converter for offshore wind energy systems," *IEEE Transactions on Power Electronics*, vol. 30, no. 2, pp. 644–656, 2015.

[17] L. Max, *Design and control of A DC grid for offshore wind farms*, Ph.D. dissertation, Department of Energy and Environment, Chalmers University of Technology, Göteborg, Sweden, 2009.

[18] R. Lenke, *A contribution to the design of isolated DC-DC converters for utility applications*, Ph.D. dissertation, Institute for Power Electronics and Electrical Drives, RWTH Aachen University, Aachen, Germany, 2012.

[19] K. Park and Z. Chen, "Analysis and design of a parallel-connected single active bridge DC-DC converter for high-power wind farm applications," in *Proceedings of 15th European Conference on Power Electronics and Applications (EPE)*, vol. 110, Lille, France, September 2013.

[20] D. Duji, F. Kieferndorf, and F. Canales, "Power electronic transformer technology for traction applications—an overview," in *Proceedings of 7th International Power Electronics and Motion Control (PEMC)*, vol. 16, no. 1, p. 5056, Daegu, Korea, June2012.

[21] M. Steiner and H. Reinold, "Medium frequency topology in railway applications," in *Proceedings of European Conference on Power Electronics and Applications (EPE)*, Aalborg, Denmark, September 2007.

[22] H. Hoffmann and B. Piepenbreier, "Medium frequency transformer in resonant switching dc/dc-converters for railway applications," in *Proceedings of 2011 14th European Conference on Power Electronics and Applications*, pp. 1–8, Birmingham, UK, August-September 2011.

[23] L. Heinemann, "An actively cooled high power, high frequency transformer with high insulation capability," in *Proceedings of APEC Seventeenth Annual IEEE Applied Power Electronics Conference and Exposition*, vol. 1, Los Cabos, Mexico, 2002.

[24] J. W. Kolar and G. I. Ortiz, "Solid state transformer concepts in traction and smart grid applications schedule/outline," in

Proceedings of 15th International Power Electronics and Motion Control Conference EPE-PEMC, pp. 1–166, Novi Sad, Serbia, September 2012.

[25] C. Dincan, P. Kjaer, Y. H. Chen, S. Munk-Nielsen, and C. L. Bak, "Analysis of a high power, resonant DC-DC converter for DC wind turbines," *IEEE Transactions on Power Electronics*, vol. 33, no. 9, pp. 7438–7454, 2017.

[26] Report 9639–01–R0, *MVDC Technology Study: Market Opportunities and Economic Impact*, TNEI Services Ltd., Manchester, UK, 2015.

[27] M. Barnes and A. Beddard, "Voltage source converter HVDC links–the state of the art and issues going forward," *in Energy Procedia*, vol. 24, pp. 108–122, 2012.

[28] F. F. Da Silva and C. L. Bak, *Electromagnetic Transients in Power Cables*, Springer, London, UK, 2013.

[29] *Cigré WG B4.57: Guide for the Development of Models for HVDC Converters in a HVDC Grid*, CIGRE Technical Brochure, Paris, France, 2014.

[30] Manitoba HVDC Research Centre, *USER'S GUIDE on the Use of PSCAD*, Manitoba HVDC Research Centre, Division of Manitoba Hydro International Ltd., Manitoba, ON, Canada, 2018.

[31] J. Beerten, S. D'Arco, and J. A. Suul, "Cable model order reduction for HVDC systems interoperability analysis," in *11th IET International Conference on AC and DC Power Transmission*, pp. 1–10, Birmingham, UK, February 2015.

[32] C. L. Bak, *Power System Technical Performance Issues Related to the Application of Long HVAC Cable*, WG C4.502s, Cigré Technical brochure, Paris, France, 2013.

[33] J. B. Glasdam, L. H. Kocewiak, J. Hjerrild, and C. L. Bak, "Control system interaction in the VSC-HVDC grid connected offshore wind power plant," in *Proceedings of Cigré Symposium 2015*, pp. 142–149, Lund, Sweden, 2015.

[34] L. Kocewiak, *Harmonics in large offshore wind farms*, Ph.D. dissertation, Aalborg University, Aalborg, Denmark, 2012.

[35] V. Preciado, "Harmonics in a wind power plant," in *Proceedings of IEEE Power and Energy Society General Meeting*, pp. 1–5, Denver, CO, USA, July 2015.

[36] K. M. Hasan, K. Rauma, A. Luna, J. I. Candela, and P. Rodriguez, "Harmonic resonance study for wind power plant," in *Proceedings of International Conference on Renewable Energies and Power Quality (ICREPQ'12)*, Santiago de Compostela, Spain, March 2012.

[37] Y. Fillion and S. Deschanvres, "Background harmonic amplifications within offshore wind farm connection projects," in *Proceedings of Power Systems Transient (IPST 2015)*, Cavtat, Croatia, June 2015.

[38] F. Mura, C. Meyer, and R. W. De Doncker, "Stability analysis of high-power dc grids," *IEEE Transactions on Industry Applications*, vol. 46, no. 2, pp. 584–592, 2010.

[39] A. Shafiu, A. Hernandez, F. Schettler, J. Finn, and E. Jørgensen, "Harmonic studies for offshore windfarms," in *Proceedings of 9th IET International Conference on AC and DC Power Transmission (ACDC 2010)*, pp. 1–6, London, UK, October 2010.

[40] B. Badrzadeh, M. Gupta, N. Singh, A. Petersson, L. Max, and M. Hogdahl, "Power system harmonic analysis in wind power plants—Part I: study methodology and techniques," in *Proceedings of Industry Applications Society Annual Meeting (IAS)*, Las Vegas, NV, USA, October 2012.

[41] PSCAD, *PSCAD/EMTDC On-Line Help System*, HVDC Research Centre, Manitoba, ON, Canada, 2013.

[42] R. J. King and T. A. Stuart, "Small-signal model for the series resonant converter," *IEEE Transactions on Aerospace and Electronic Systems*, vol. AES-21, no. 3, pp. 301–319, 1985.

[43] X. Wang, F. Blaabjerg, and W. Wu, "Modeling and analysis of harmonic stability in an AC power-electronics-based power system," *IEEE Transactions on Power Electronics*, vol. 29, no. 12, pp. 6421–6432, 2014.

[44] B. Gustavsen and A. Semlyen, "Rational approximation of frequency domain responses by vector fitting," *in IEEE Transactions on Power Delivery*, vol. 14, no. 3, pp. 1052–1061, 1999.

[45] J. R. Marti, "Accuarte modelling of frequency-dependent transmission lines in electromagnetic transient simulations," *IEEE Transactions on Power Apparatus and Systems*, vol. PAS-101, no. 1, pp. 147–157, 1982.

[46] Y. H. Chen, C. G. Dincan, P. C. Kjær, C. L. Bak, X. Wang, and C. E. Imbaquingo, "Model-based control design of series resonant converter based on the discrete time domain modelling approach for DC wind turbine," *Journal of Renewable Energy*, vol. 2108, Article ID 7898679, 18 pages, 2018.

[47] C. Imbaquingo, N. Isernia, E. Sarrà, and A. Tonellotto, "Modelling DC collection of offshore wind farms for harmonic susceptibility study," May 2017, https://www.dcc.et.aau.dk/digitalAssets/390/390654_aau-2017-carlos-dc-harmonics-on-src-converter.pdf.

[48] R. W. Erickson and D. Maksimovic, *Fundamentals of Power Electronics*, Springer Science & Business Media, Berlin, Germany, 2007.